Fluid–Melt–Rock Interaction during the Transition from Magmatism to HT-UHT-Granulite- and Amphibolite-Facies Metamorphism in the Ediacaran Adrar–Suttuf Metamafic Complex, NW Margin of the West African Craton (Southern Morocco)

JOSÉ FRANCISCO MOLINA [iD][1,*], FERNANDO BEA [iD][1], PILAR MONTERO[1], FAOUZIYA HAISSEN[2], LETICIA BARCOS[1], AITOR CAMBESES[1], IRENE MORALES[1], MARIA MONIKA REPCZYNSKA[1], OTHMAN SADKI[3] and ANTONIO GARCÍA-CASCO[1]

[1]Departamento de Mineralogía y Petrología, Universidad de Granada, Campus Fuentenueva, 18071 Granada, Spain
[2]Département de Géologie, Faculté des Sciences Ben Msik, Université Hassan-II, B.P. 7955 Casablanca, Morocco
[3]Office National des Hydrocarbures et des Mines, 5, avenue Moulay-Hassan, B.P. 99 Rabat, Morocco

*Corresponding author. E-mail: jfmolina@ugr.es

Underplated mafic intrusions ponded at the base of the lower continental crust in extensional settings can experience ultra-high-temperature (UHT) granulite-facies metamorphism during tens of My due to slow cooling rates. These intrusions are also the source of heat and carbonic fluids for regional high-temperature (HT) granulite-facies metamorphism in the continental crust. This work analyses the fluid–melt–rock interaction processes that occurred during the magmatic to HT-UHT-granulite- and amphibolite-facies metamorphic evolution of high-grade mafic rocks from the Eastern Ediacaran Adrar–Suttuf Metamafic Complex (EASMC) of the Oulad Dlim Massif (West African Craton Margin, Southern Morocco). P–T conditions were determined using Ti-in-amphibole thermometry, two-pyroxene and amphibole–plagioclase thermobarometry, and phase diagram calculations. The thermobarometric study reveals the presence of tectonically juxtaposed lower- and mid-crustal blocks in EASMC that experienced decompression-cooling paths from, respectively, UHT and HT granulite-facies conditions at ca. 1.2 ± 0.28 GPa and $975 \pm 50°C$, and ca. 0.82 ± 0.15 GPa and $894 \pm 50°C$, to amphibole-facies conditions at ca. 0.28 ± 0.28 GPa and $787 \pm 45°C$ (precision reported for the calibrations at 1 s level). An age for the magmatic to UHT granulite-facies metamorphic transition of 604 Ma was constrained from published SHRIMP Th–U–Pb zircon ages of the igneous protoliths. An amphibole ^{40}Ar–^{39}Ar cooling age of 499 ± 8 Ma (precision at 2 s level) was obtained for the lower-crustal blocks. Amphibole ^{40}Ar–^{39}Ar closure temperatures of 520–555°C were obtained for an age range of 604–499 Ma and an average constant cooling rate of 4.2°C/My, suggesting that the lower-crustal blocks cooled down to the greenschist–amphibolite facies transition in ca. 100 My. During the high-temperature stage, interstitial hydrous melts assisted textural maturation of the rock matrix and caused incongruent dissolution melting of olivine and pyroxenes, and, probably, development of An-rich spikes at the grain rims of plagioclase, and local segregation of pargasite into veins. Subsequent infiltration of reactive hydrous metamorphic fluids along mineral grain boundaries during cooling down to amphibole-facies conditions promoted mineral replacements by coupled dissolution-precipitation mechanisms and metasomatism. Ubiquitous dolomite grains, with, in some cases, evidence for significant textural maturation, appear in the granoblastic aggregates of the high-grade mafic rocks. However, calculated phase relationships reveal that dolomite could not coexist with H_2O–CO_2 fluids at HT-UHT granulite- and low-medium P amphibolite-facies conditions. Therefore, it is proposed that it may have been generated from another CO_2-bearing phase, such as an immiscible carbonatitic melt exsolved from the parental mafic magma, and preserved during cooling due to the prevalence of fluid-absent conditions in the granoblastic matrix containing dolomite. The lower-crustal mafic intrusions from EASMC can represent an example of a source of heat for granulitisation of the mid crust, but a sink for carbon due to the apparent stability of dolomite under fluid-absent conditions.

Key words: Amphibole–plagioclase thermobarometry; ^{40}Ar–^{39}Ar geochronology; Ediacaran Adrar–Suttuf Metamafic Complex; fluid–melt–rock interaction; UHT granulite-facies metamorphism

INTRODUCTION

Ultra-high-temperature (UHT) metamorphism, characterised by temperatures over 900°C, has been described in many granulite-facies terranes across the world (e.g. Harley, 1998; Harley, 2004, 2008; Kelsey, 2008; Clark et al., 2011; Kelsey & Hand, 2015; Pownall, 2015; Harley, 2016; Touret et al., 2016; Lei & Xu, 2018). High-temperature (HT) and UHT granulites can be generated in a large diversity of tectonic settings including, among others, continental rifts, collisional orogens, and oceanic and continental arcs (e.g. Warren, 1983; Sandiford & Powell, 1986; Bohlen, 1991; Gibson & Ireland, 1995; Müntener et al., 2000; Schmitz & Bowring, 2003;

Harley, 2004, 2008; Petterson, 2010; Touret & Huizenga, 2012; Kelsey & Hand, 2015; Cipar et al., 2020; Touret & Huizenga, 2020; Dharmapriya et al., 2021; Touret et al., 2022).

The role of fluids during the amphibolite-granulite transition and crustal anatexis is still under intense debate being proposed scenarios varying from fluid-absent (e.g. Stevens & Clemens, 1993; Clemens et al., 2016) to fluid-present conditions with the appearance of CO_2 and saline fluids, even with high-H_2O activities, that percolate the continental crust at granulite-facies conditions (e.g. Aranovich et al., 2014, 2016; Newton et al., 2014). Fluid infiltration can promote metasomatism (e.g. Touret & Huizenga, 2012; Harlov & Austrheim, 2013; Touret & Nijland, 2013; Touret et al., 2019), melting (e.g. Stuart et al., 2017, 2018; Touret et al., 2022) as well as profound mineralogical and textural transformations (Putnis & Austrheim, 2013; Putnis et al., 2017) and changes in the composition of magmas ascending from the mantle to the mid crust, e.g. contamination of vaugnerites (mostly biotite-rich diorites, quartz diorites, and quartz monzodiorites; Le Maitre, 1989) with supercritical fluids produced by biotite breakdown (Bea et al., 2021).

One of the sources of fluids that assist the transformation of the continental crust into granulites (i.e. granulitisation processes that involve both blastesis of HT and UHT diagnostic mineral assemblages and intense textural maturation that gives rise to granoblastic aggregates) is degassing of underplated magmas that pond at the base of the lower crust. These magmas also provide a heat source to maintain high thermal regimes over millions of years to achieve UHT granulite-facies conditions (e.g. Frost et al., 1989; Huppert & Sparks, 1989; Frost & Frost, 2008; Newton, 2020). Therefore, the study of lower-crustal mafic intrusions, which transform themselves into granulites upon slow cooling, can thus provide important constraints on: (i) fluid–melt–rock interaction processes at the magmatic to metamorphic transition and during subsequent cooling (e.g. Wang et al., 2022; Müntener et al., 2000; Torres-Rodriguez et al., 2021; Munnikhuis et al., 2023; Tribuzio et al., 2023); (ii) degassing of magmas sourced from the mantle (e.g. Frost & Frost, 2008; Blanks et al., 2020; Newton, 2020; Touret & Huizenga, 2020); and (iii) duration of the UHT metamorphism recorded in their mineral assemblages and the relevance as a heat source for granulitisation of the middle crust (e.g. Frost et al., 1989; Harley, 2016). To this end, it is necessary to establish the P–T–t evolution of these deep-seated complexes. However, determining reliable P–T conditions in these hot, slowly cooled complexes is challenging. Thus, the use of classical thermobarometry is hampered by resetting of mineral compositions on cooling, especially those of pyroxenes due to the development of exsolution lamellae and the Mg–Fe^{2+} exchange between ferromagnesian minerals (e.g. Lindsley, 1983; Frost & Chacko, 1989; Pattison et al., 2003; Ray et al., 2021). Besides, the computation of equilibrium assemblage diagrams is limited by the complex thermodynamic treatment of multicomponent phases and the uncertainty in the system composition, which may have been modified by migration of reactive melts or metasomatic fluids (e.g. Touret & Huizenga, 2012; Putnis & Austrheim, 2013; Touret & Nijland, 2013; Forshaw et al., 2019; Newton, 2020; Molina et al., 2021). However, amphibole–plagioclase thermobarometry (Holland & Blundy, 1994; Molina et al., 2015, 2021) and Ti-in-amphibole thermometry (Otten, 1984; Liao et al., 2021) might give more promising results because the composition of Ti amphibole and binary plagioclase from plutonic and high-grade metamorphic rocks can be preserved during slow cooling (Otten, 1984; Anovitz, 1991; Drüppel et al., 2001; Benisek et al., 2004; Molina et al., 2009; Sajeev et al., 2009; Liao et al., 2021). The results obtained by these methods can be combined with

two-pyroxene thermobarometry on both reintegrated and reset compositions to get more reliable P–T determinations and a better understanding of the petrogenetic processes.

The Adrar–Suttuf Metamafic Complex (ASMC), exposed in the central region of the Oulad Dlim Massif (ODM), western margin of the Reguibat Rise (Southern Morocco) (Figs. 1a-b), contains large mafic igneous intrusions emplaced in the lower crust. They were generated during an Ediacaran rift-related basic magmatism and metamorphosed at high-P amphibolite- and granulite-facies conditions (Molina et al., 2018; Bea et al., 2020). In the eastern border of the ASMC, the granulitised mafic rocks present a large diversity of near-solidus to post-magmatic pargasite–clinopyroxene–orthopyroxene-plagioclase assemblages that permit a robust determination of their P–T conditions of equilibration, and an analysis of the reaction processes that take place during cooling of deep-seated mafic intrusions. Furthermore, a precise SHRIMP U-Pb zircon age of 604 Ma (Bea et al., 2020) for the magmatism can provide, in combination with amphibole ^{40}Ar–^{39}Ar cooling ages, important constraints on the cooling history of the intrusions.

This study aims to determine the metamorphic evolution of the high-grade mafic rocks from the eastern border of the ASMC, as well as to improve the understanding of fluid–melt–rock interaction processes that occurred during the magmatic to metamorphic transition and the slow cooling of these deep mafic intrusions. To this end, we have performed a detailed textural and mineralogical analysis of high-grade mafic rocks from the Entajate and Mades bodies, located on the eastern border of the ASMC (Fig. 1c). Their equilibrium P–T conditions were determined using amphibole–plagioclase thermobarometry (Molina et al., 2015, 2021), two-pyroxene thermobarometry (Putirka, 2008) and Ti-in-amphibole thermometry (Liao et al., 2021). The P–T stability fields determined for the mineral assemblages from the mafic rocks were tested by thermodynamic modelling using the GeoPS program (Xiang & Connolly, 2022). New amphibole ^{40}Ar–^{39}Ar geochronological data are used to determine the cooling ages and the closure temperatures of these deep intrusions, using constraints for initial ages from zircon Th–U–Pb dating reported in Bea et al. (2020).

GEOLOGICAL SETTING AND FIELD RELATIONSHIPS

The Oulad Dlim Massif (ODM), exposed over an area of ca. 36 000 km^2, constitutes an Archean to late Paleozoic metamorphic collage of complexes located to the west of the Reguibat Shield (Fig. 1a), between latitude 21° 24′ N to N 23° 30′ N and longitude 14° 36′ W to W16° 18′ W, and forms, along with the Dhlou–Zemmour and Mauritanide belts, the western pericratonic domain of the Reguibat Shield (e.g. Sougy, 1962a, 1962b; Lécorché et al., 1991; Villeneuve et al., 2006; Michard et al., 2008, 2010; Montero et al., 2014, 2018; Molina et al., 2018; Bea et al., 2020). A revision of the geochronology and geochemistry of the magmatism from the Tichla–Awsard domain of the Reguibat Shield, and from the Western Reguibat Alkaline Province can be found in Bea et al. (2013, 2014, 2016), Montero et al. (2014, 2016, 2018) and Haissen et al. (2016, 2018).

Villeneuve et al. (2015) (see also Gärtner et al., 2013, 2016) proposed that the ODM (named by them 'Adrar Suttuf'; term that in the present work refers only to the mafic part of the massif) represents a Pan-African belt that includes a Neoproterozoic island-arc reworked during the Variscan collision of the West African Craton with the North American Craton. However,
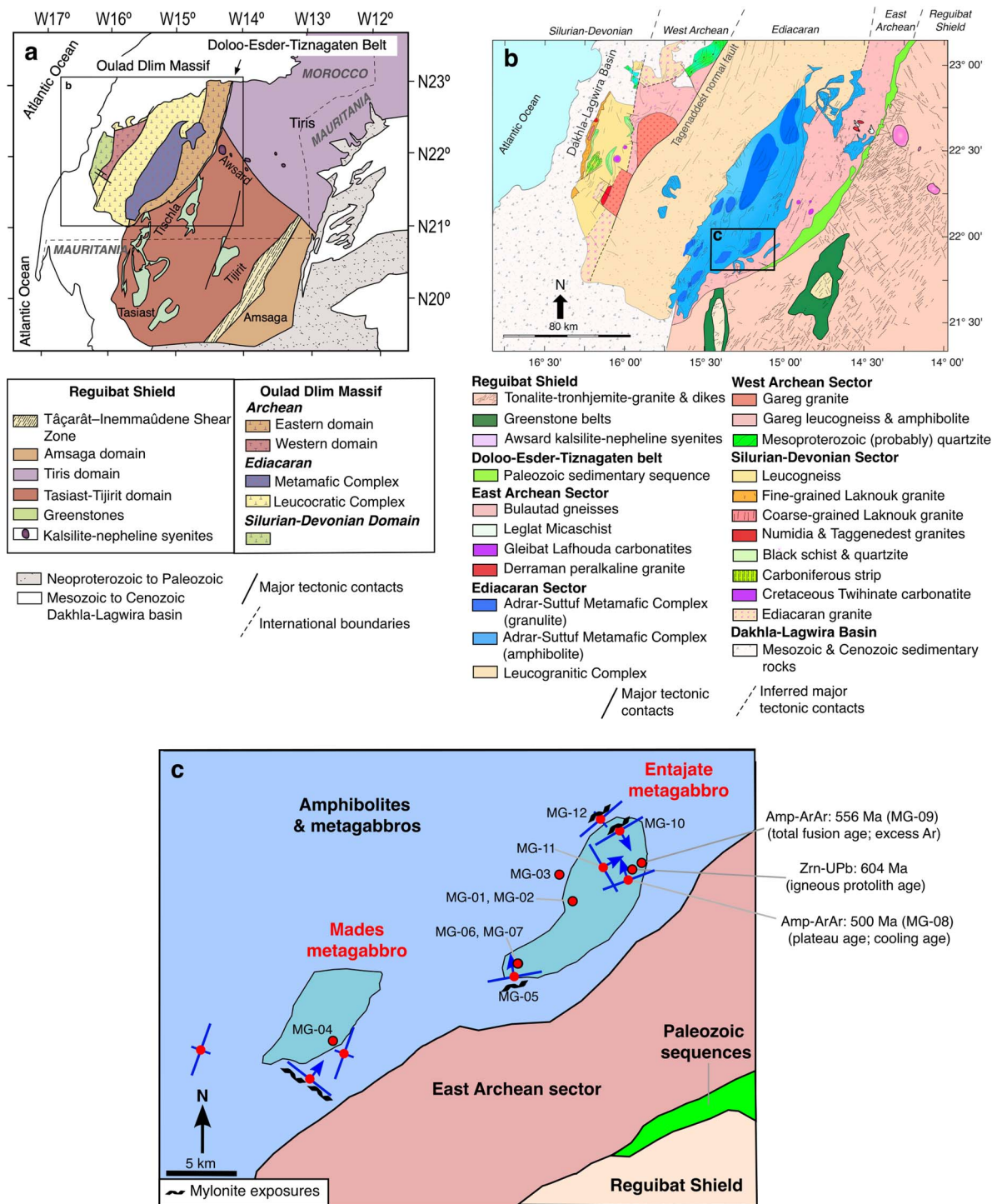
Fig. 1. (a) Geological map of the Western Reguibat Shield with the location of the Oulad Dlim Massif (Southern Morocco). (b) Geological map of the Oulad Dlim Massif. (c) Location of samples studied in this work. (a and b reprinted from Bea *et al., 2020*, with permission from Elsevier).

recently Bea *et al.* (2020) have challenged this model, proposing that the ODM is constituted by an Archean terrain, divided by an Ediacaran intracontinental rift that produced a voluminous bimodal mafic-felsic magmatism, and a Silurian-Devonian granite belt situated at the westernmost end of the massif (Fig. 1b). Accordingly, these authors have distinguished two domains in the Archean terrain: the Eastern and the Western Archean Sectors. The Eastern Archean Sector overthrust the Paleozoic sedimentary rocks of the Doloo-Esder-Tiznagaten belt, situated at the boundary between the Oulad Dlim Massif and the Reguibat Shield, along its

eastern margin (Sougy, 1962b; Figs. 1a, b). The Western Archean Sector is bounded to the west by the Silurian-Devonian Sector. The Ediacaran Sector is exposed between these two Archean domains; it is composed of two contrasting lithodemic units that, however, share a common, seemingly gradational, contact: the Adrar–Suttuf Metamafic Complex (ASMC) and the Leucocratic Gneiss Complex (LGC). The former overthrust the Eastern Archean Sector at its eastern margin, while the latter is bounded to the west by the Western Archean Sector through the NNE-trending Tagenaddest normal fault (Bea *et al., 2020*; Fig. 1b). At their northernmost end,
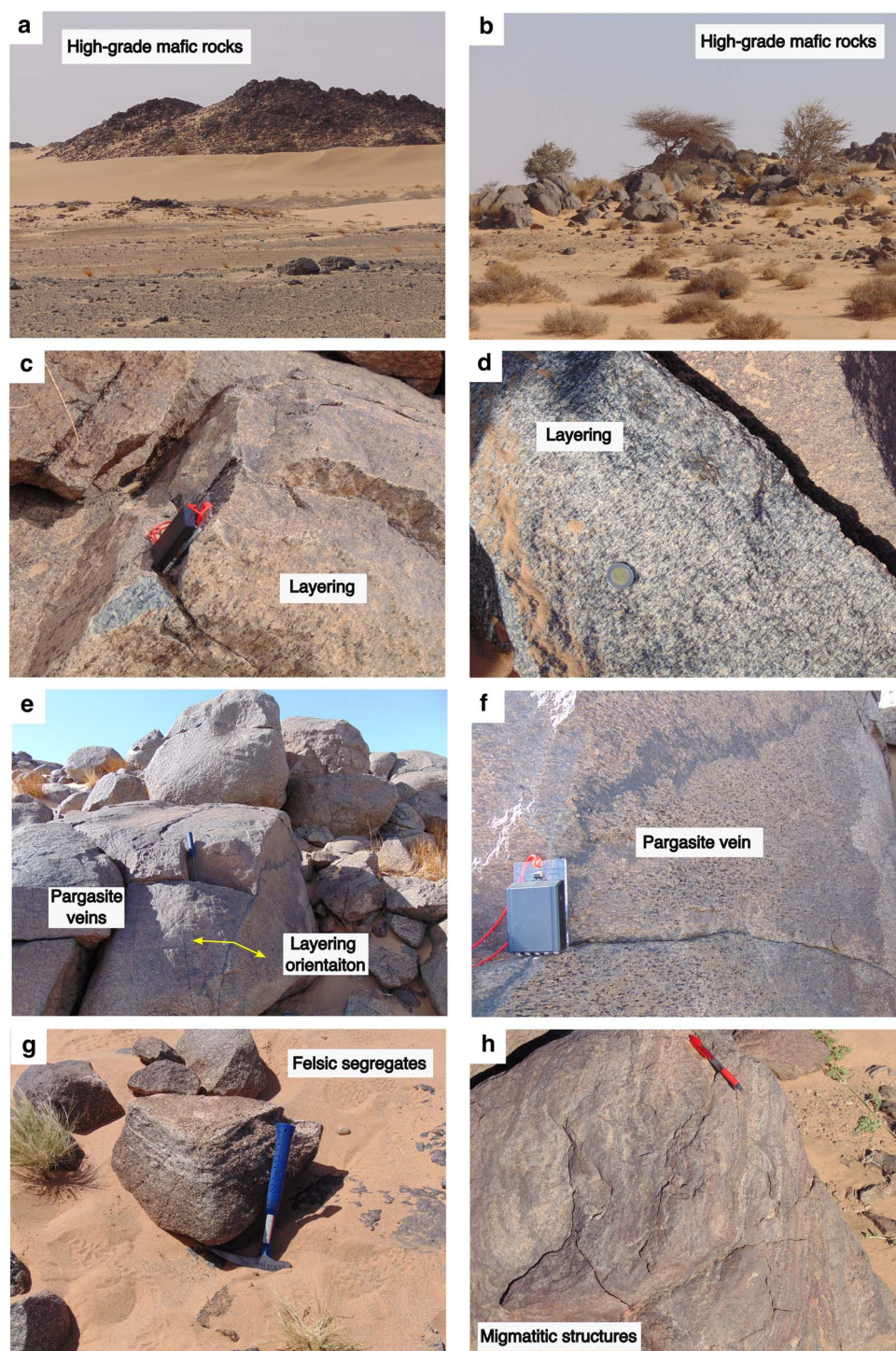
Fig. 2. Field relationships of high-grade mafic rocks from the Adrar–Suttuf Metamafic Complex. (a and b) Photographs of high-grade mafic rock exposures. Views of hills and small mounds of metagabbros and mafic granulites, much more resistant to erosion than the surrounding amphibolites, standing out on vast plains partially covered with desert sand. (c and d) Layering defined by alternating centimetre-scale felsic and mafic bands in Ol-metagabbro. (e) Ol-metagabbros with pargasite veins cutting its layering obliquely. (f) Close-up of the vein. (g) Anorthositic segregations in mafic granulites. (h) Migmatitic structures in charnockites from the western border of the Adrar–Suttuf Metamafic Complex.

the transitional contact between these roughly parallel NNE-trending Ediacaran units is rotated and intricately folded (Fig. 1b).

The Adrar–Suttuf Metamafic Complex consists of a vast exposure of foliated amphibolites, granulitised mafic rocks and minor metasedimentary rocks (mostly marbles and calc-silicate rocks). The igneous protoliths of the amphibolites and high-grade mafic rocks have been dated by Bea *et al.* (2020) using the SHRIMP

Th–U–Pb zircon method. The results show that they are coeval and have a gradual age variation from about 604 Ma in the east to ca. 584 Ma in the west (Bea *et al.*, 2020). The amphibolites and high-grade mafic rocks show a restricted silica range (44–54 wt % SiO_2) and a bimodal distribution of the Mg-number that defines two compositional series that occurs in distinct geographic positions (Bea *et al.*, 2020): a magnesian series, depleted in incompatible

elements, is located in the east and a ferroan series with tholeiitic affinity, less depleted in incompatible elements, occurs mostly, but not exclusively, in the west. The high-grade mafic rocks mainly consist of metacumulates with pargasite + plagioclase + clinopyroxene + orthopyroxene ± olivine in the magnesian series, and metagabbroic rocks with pargasite + plagioclase + clinopyroxene + orthopyroxene ± Fe-Ti oxides in the ferroan series. The chemical and isotopic compositions of the two mafic rock series and the spatially- and temporally-associated granites from the LGC suggest that they represent a bimodal magmatism generated in a continental rift (Bea *et al.,* 2020).

The granulitised mafic rocks occur as enclaves within the amphibolite sequences, often appearing as distinct mappable bodies (Fig. 1b), such as those of Entajate and Mades on the eastern border of the ASMC (Fig. 1c). These bodies, significantly more resistant to erosion than the surrounding amphibolites, form hills and small mounds that protrude from vast plains, which are partially covered with desert sand and rocky detritus (Figs. 2a, b). The most common petrographic types are metagabbronorites, which can contain either olivine in the high-Mg-number series or quartz in the more ferrous compositions, and meta-anorthosites, some of them pegmatitic. Rare bodies of metamorphosed charnockites s.s. are found in the westernmost end of the complex (Bea *et al.,* 2020). The high-grade mafic rocks can be massive or layered, presenting a millimetric to centimetric banding of alternating plagioclase and mafic minerals (Figs. 2c, d). Notably, veins of pargasite cross-cut the layering locally (Figs. 2e, f). Anorthositic segregations and migmatitic structures have also been reported in, respectively, mafic granulites and charnockites (Figs. 2g-h) suggesting that they experienced partial melting during the high-grade metamorphic event, as discussed in Bea *et al.* (2020). The contacts between the high-grade mafic rock bodies and the amphibolites are highly sheared, resulting in the development of a mylonitic banding in the former (Fig. 3a). The shear deformation produced transposition of the pargasite veins (Fig. 3b), thus indicating that there was a high-temperature veining process before shearing. Besides, intense retrogression of the mafic rocks is observed adjacent to later veins of Cl-bearing amphibole (Fig. 3c; see below for a discussion).

MINERAL TRANSFORMATION DURING EVOLUTION FROM HT-UHT GRANULITE- TO AMPHIBOLITE-FACIES CONDITIONS
Sample description

A total of 12 samples from the Eastern Adrar–Suttuf Metamafic Complex (EASMC) were selected for this study, (Fig. 1c; see Appendix A in Molina *et al.,* 2024, for mineral modal abundances; mineral abbreviations after Whitney & Evans, 2010): two samples of meta-anorthosite (samples MG-10 and MG-11: 82–84 vol % Pl, 3–4 vol % Amp, ca. 3 vol % Cpx, 6–10 vol % Opx, and < 3 vol % Ol), one sample of metaleucogabbronorite (sample MG-12: 56 vol % Pl, 14 vol % Amp, 19 vol % Cpx, and 11 vol % Opx), five samples of Ol metaleucogabbronorite (samples MG-02, MG-04, MG-06, MG-08, and MG-09: 58–70 vol % Pl, 5–15 vol % Amp, 4–20 vol % Cpx, 3–10 vol % Opx, and 4–20 vol % Ol), three samples of metagabbronorite (samples MG-01, MG-03, and MG-05: 32–41 vol % Pl, 11–16 vol % Amp, 19–50 vol % Cpx, and 4–20 vol % Opx) and one sample of Ol metagabbronorite (sample MG-07: 42 vol % Pl, 10 vol % Amp, 14 vol % Cpx, 22 vol % Opx, and 10 vol % Ol). The accessory minerals are ubiquitous dolomite, coarse-grained spinel, which is only present in Ol-bearing lithotypes, ± magnetite ± ilmenite, sulphides (pyrite, chalcopyrite, and pentlandite), and
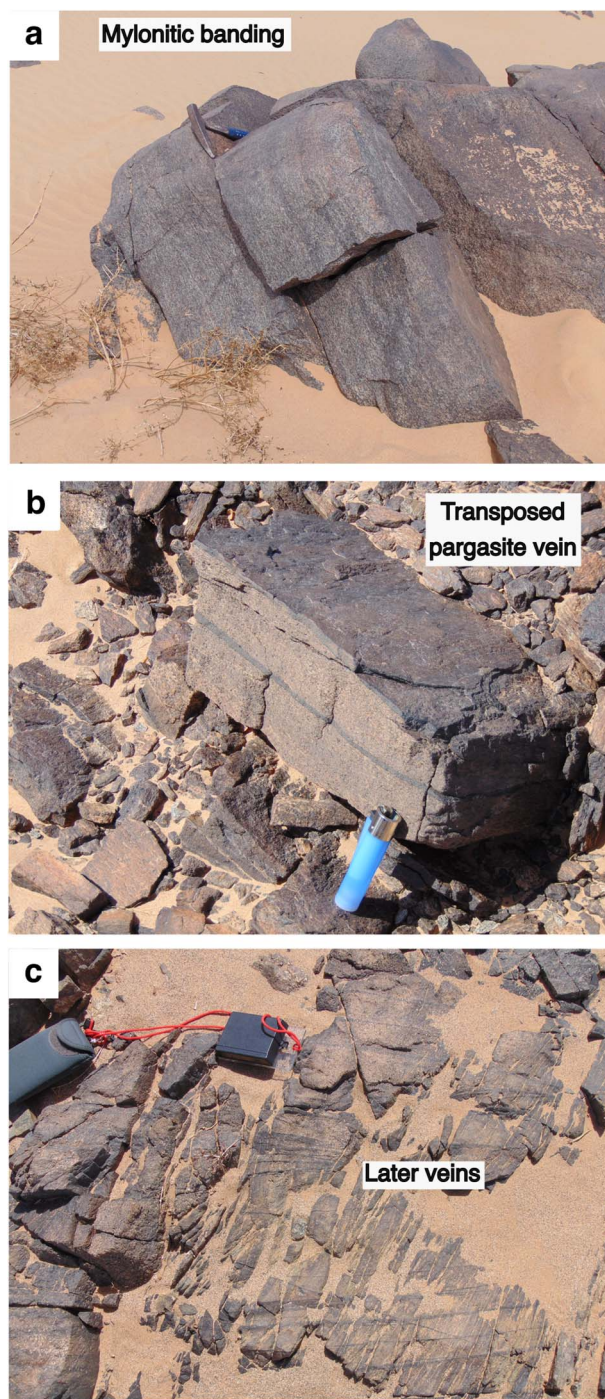

Fig. 3. Field relationships of high-grade mafic rocks from the Eastern Adrar–Suttuf Metamafic Complex. (a) Intensely deformed mafic granulite presenting a mylonitic banding. (b) Intensely deformed mafic granulite with a Ti pargasite vein transposed to the mylonitic banding. (c) Late Cl amphibole veins with intense retrogression of the mafic rock.

very scarce garnet and corundum that only appear in sample MG-10. A large variety of symplectitic aggregates, described later, are present in all rock types.

Nine samples (MG-01, MG-02, MG-03, MG-04, MG-06, MG-07, MG-08, MG-09, and MG-11) come from the inner parts of the high-grade mafic bodies (Fig. 1c) and show granoblastic aggregates with variable degrees of textural maturation. Among these, seven samples (MG-02, MG-04, MG-06, MG-07, MG-08, MG-09, and

MG-11) present relicts of olivine partially replaced by coronas of orthopyroxene of probable igneous origin, as discussed later, and are henceforth referred to as *Ol-metagabbros* to highlight the presence of this igneous texture; the remaining two samples (MG-01 and MG-03) are designated as *mafic granulites*. Additionally, three samples (MG-05, MG-10, and MG-12) come from the borders of these bodies and exhibit mylonitic fabrics, thus referred to as *mylonitic mafic granulites*.

Mineral microanalysis and SEM images

Minerals analyses were performed by wavelength dispersive spectrometry (WDS) using a CAMECA SX100 electron microprobe at the Centro de Instrumentación Científica (CIC, University of Granada, Spain) operated at 20 kV accelerating voltage and 20 nA beam current. Both natural and synthetic standards were used for the calibration: diopside (Si), hematite (Fe), wollastonite (Ca), albite (Na), sanidine (K), rutile (Ti), rhodonite (Mn), vanadinite (Cl), fluorite (F), and synthetic periclase (Mg), Al_2O_3 (Al), Cr_2O_3 (Cr), and NiO (Ni). The precision was close to 4% for an analyte concentration of 1 wt %. Mineral analyses were also carried out by energy dispersive spectroscopy (EDS) using a ZEISS EVO-10 high-vacuum scanning electron microscope (HV-SEM) at the CIC operated at 15 kV, using natural mineral standards. The original pre-exsolution compositions of clinopyroxene and orthopyroxene were reintegrated by EDS raster analysis of rectangular areas with edges ranging from 40 to 300 μm. Back-scattered electron (BSE) images were also captured with the ZEISS EVO-10 HV-SEM (see Appendix B in Molina *et al.,* 2024, for representative BSE-SEM images and microphotographs with location of spot and areal analyses).

Selected mineral compositions are listed in Appendixes C and D (Molina *et al.,* 2024). Fe^{3+} and Fe^{2+} contents in amphibole (normalisation to 23 O), garnet (normalisation to 12 O), ilmenite (normalisation to 3 O), pyroxenes (normalisation to 6 O), spinel-group minerals (normalisation to 4 O) were calculated by charge balances and stoichiometric constraints. A modified version of the average Fe^{3+} method of Spear & Kimball (1984), described in Appendix A from Dale *et al.* (2005), was used for the amphibole formula, assuming $OH + Cl + F = 2$ atoms per formula unit, apfu. Mineral formulas were calculated assuming total Fe as Fe^{2+} for carbonates (normalisation to 3 O), olivine (normalisation to 4 O), and plagioclase (normalisation to 8 O).

Mineral assemblages

The high-grade mafic rocks present a main mineral assemblage consisting mostly of pargasite/hornblende $\pm$ clinopyroxene + orthopyroxene + labradorite/bytownite + dolomite $\pm$ spinel $\pm$ Fe-Ti oxides. This mineral assemblage forms granoblastic aggregates with different degrees of textural maturation and evidence for the presence of a former interstitial melt, thus suggesting mineral equilibration during a transition from magmatic to metamorphic conditions. During cooling, this high-temperature texture was overprinted by various types of symplectitic aggregates and cross-cut by late veins that witness fluid–rock interaction processes along grain boundaries and fractures. Besides, the high-grade mafic bodies were intensely sheared at their borders, resulting in the development of mylonitic fabrics that provide relative time constraints on the sequence of processes occurring during cooling.

Below, a detailed description is provided of the textural and mineralogical imprints resulting from melt- and fluid-mediated reaction processes on the EASMC high-grade mafic rocks. The main textual criterion used for distinguishing between these two

reaction mechanisms is the formation of micropores, characterised by their rounded shapes, in the mineral products resulting from replacement processes caused by dissolution-precipitation mechanisms assisted by fluids (c.f., Putnis, 2002, 2009; Putnis & Austrheim, 2013; Spruzeniece *et al.,* 2017). These mechanisms differ from those involving melts in that the latter would lead to the formation of melt inclusions in the mineral products, which would crystallise during slow cooling (see Putnis, 2002, for further discussion).

Melt-mediated reaction processes during magmatic to metamorphic transition
Textural maturation in the presence of interstitial residual melts

The rock matrix of Ol-metagabbros and mafic granulites is characterised by medium- to coarse-grained granoblastic aggregates of amphibole, clinopyroxene, orthopyroxene, plagioclase, dolomite, spinel and Fe-Ti oxides (Figs. 4a-c). The composition of *amphibole* from these aggregates is pargasite and Ti pargasite (compositional ranges: $Ti = 0.13–0.37$ apfu (23 O), $AlIV = 1.70–2.12$ apfu, A-site (Na + K occupancy in A site) = 0.68–0.95 apfu, and $Mg/(Mg + Fe^{2+}) = 0.64–0.82$ in Ol-metagabbros; $Ti = 0.20–0.31$ apfu, $AlIV = 1.86–2.01$ apfu, A-site = 0.71–0.84 apfu, and $Mg/(Mg + Fe^{2+}) = 0.62–0.74$ in mafic granulites; Figs. 5a-c). The Cl occupancy is very low (<0.02 apfu; $X_{Cl} < 0.017$, $X_i = i/(F + Cl + OH)$; $i = F, Cl$; Fig. 5d), while that of F is higher (up to 0.15 apfu; $X_F < 0.075$), but still much lower than that reported in pargasite formed by infiltration of F-bearing fluids, such as this from the Archean Napier Complex, which can achieve X_F values of up to 0.48 (Tsunogae *et al.,* 2003). The amphibole grains show no exsolution lamellae suggesting negligible compositional resetting upon cooling. In some samples (e.g. MG-01, MG-03, MG-08, MG-09, and MG-11), they present a typical cooling compositional path characterised by decreasing in Ti occupancy and increasing in $Mg/(Mg + Fe^{2+})$ ratio (Figs. 6a-b) (c.f., Czamanske & Wones, 1973; Molina *et al.,* 2009). By contrast, the *clinopyroxene* grains from the granoblastic aggregates experienced a significant compositional resetting that is evidenced by the appearance of exsolution lamellae of orthopyroxene at their cores; the rims can be devoid of exsolutions suggesting overgrowth at lower temperature conditions (Fig. 4c). Reintegrated compositions of grain cores are mostly diopside (compositional ranges: $Al = 0.17–0.21$ apfu (6 O), $Ca = 0.83–0.86$ apfu, CaTs (Ca-tschermak (%) = 100 [AlVI-Na]) = 3–7 mol %, and $Mg/(Mg + Fe^{2+}) = 0.78–0.87$ in Ol-metagabbro MG-09; $Al = 0.20–0.21$ apfu Al, $Ca = 0.84–0.85$ apfu, CaTs = 4–7 mol % and $Mg/(Mg + Fe^{2+}) = 0.83–0.87$ in mafic granulite MG-01; Figs. 7a, b). Spot analyses of grain cores and both areal and spot analyses of rims show diopside compositions with a distinctive higher Ca occupancy (> 0.86 apfu) (Fig. 7b). The *orthopyroxene* grains from the granoblastic aggregates show very tiny exsolution lamellae of clinopyroxene developed during cooling (Fig. 4d). They have reintegrated compositions of enstatite with 0.11 to 0.16 apfu (6 O) Al, 0.021 to 0.031 apfu Ca, and $Mg/(Mg + Fe^{2+})$ of 0.66 to 0.75 (samples MG-01 and MG-09; Figs. 7a and c). Spot analyses of grain cores and rims show similar compositions with 0.064 to 0.17 apfu Al, 0.007 to 0.019 apfu Ca, and $Mg/(Mg + Fe^{2+})$ of 0.66 to 0.77 (Figs. 7a and c). The *plagioclase* grain cores from the granoblastic aggregates are relatively homogeneous within each sample ranging from labradorite to bytownite with $An_{58–63}$ ($An = 100*Ca/(Ca + Na + K)$ atomic ratio) in MG-08 and MG-09, $An_{67–71}$ in MG-01 and MG-06, $An_{72–76}$ in MG-02, MG-03, and MG-11, and $An_{85–87}$ in MG-07. The *spinel* from the Ol-metagabbros has $Mg/(Mg + Fe^{2+})$ of 0.50–0.64 in grain cores, decreasing to 0.43–0.45 at the rims; its
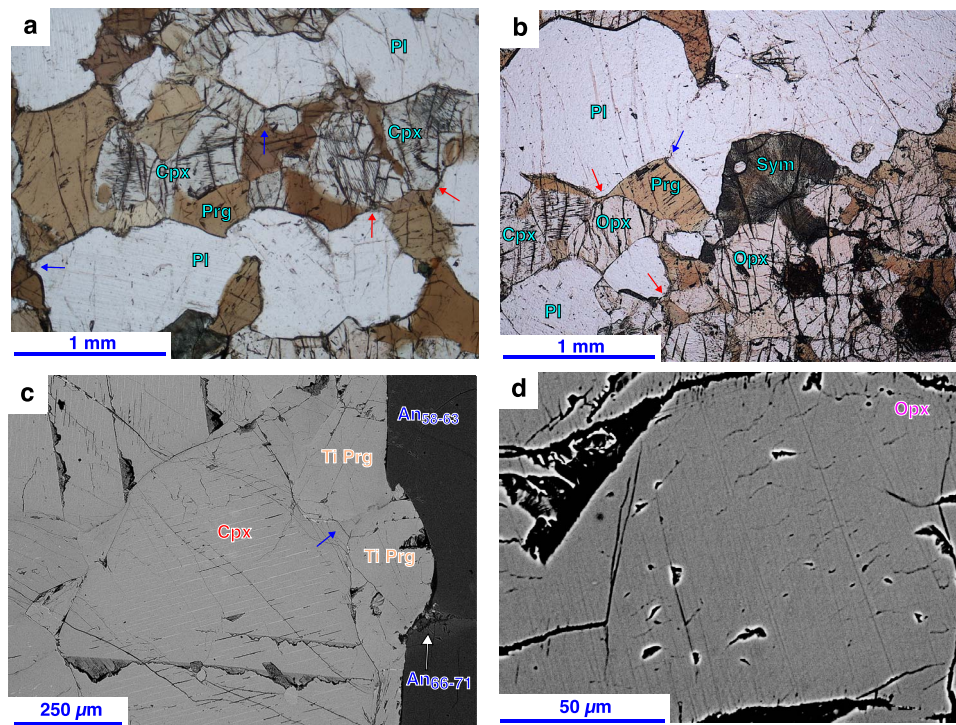
Fig. 4. Microphotographs and BSE images of high-grade mafic rocks from the Eastern Adrar–Suttuf Metamafic Complex. (a and b) Microphotographs of medium- to fine-grained granoblastic aggregates of clinopyroxene, orthopyroxene, olivine, pargasite, and plagioclase in Ol-metagabbros MG-08 (a) and MG-09 (b) with anhedral clinopyroxene grains rimmed by pargasite and blebs of pargasite. Note low dihedral angles subtended at Prg–Cpx–Cpx, Prg–Pl–Pl and Pl–Prg–Prg junctions (marked with blue arrows) and pargasite films wetting plagioclase-clinopyroxene and plagioclase-orthopyroxene grain boundaries (marked with red arrows). Plane-polarised light. (c) BSE image of medium-grained granoblastic aggregate from Ol-metagabbro MG-09 consisting of pargasite and clinopyroxene exhibiting exsolution lamellae of orthopyroxene with a low Cpx–Prg–Prg dihedral angle (marked with blue arrow) and labradorite grain with an An-rich spike (arrowed) at its rim. Note that exsolution lamellae are absent in the clinopyroxene rim wetting the pargasite-pargasite grain boundary. (d) BSE image of orthopyroxene grain from Ol-metagabbro MG-09 exhibiting very tiny exsolution lamellae of clinopyroxene. In BSE images, the colour of circles corresponds to the mineral indicated by the label with the same colour. Mineral abbreviations after Whitney & Evans (2010).

composition is similar to this from high-grade metamorphic rocks, with negligible Cr/(Cr + Al) ratios and high Al occupancies (ranges: 1.92–1.95 apfu (4 O) in grain cores and 1.89–1.91 apfu at grain rims) (Figs. 8a-b). In the granoblastic aggregates of mafic granulite MG-03, it appears *ilmenite* and *magnetite* with, respectively, 0.26–0.31 apfu (3 O) Fe^{3+} and 0.45–0.46 apfu (4 O) Ti (Fig. 8c).

The granoblastic aggregates show high apparent dihedral angles at many triple-junctions (Figs. 4a-b), implying a generalized solid-state re-equilibrium caused by an intense UHT annealing (see section on P–T estimations for details). However, dihedral angles subtended at Prg–Cpx–Cpx, Prg–Pl–Pl, Pl–Prg–Prg and Cpx–Prg–Prg junctions remain low (blue arrows in Figs. 4a-c), whereas pargasite can appear as thin films that 'wet' plagioclase-clinopyroxene and plagioclase-orthopyroxene grain boundaries (red arrows in Figs. 4a-b). This is taken as evidence for the presence of a former interstitial melt during annealing (c.f., Holness *et al.*, 2005, 2007; Stuart *et al.*, 2016; Munnikhuis *et al.*, 2023). Locally, clinopyroxene grains are partially replaced by pargasite (Figs. 4a-b) with a composition similar to that form granoblastic aggregates (Figs. 6b-c; sample MG-01), implying an incongruent dissolution that could have been caused by reaction with this interstitial melt (c.f., Beard *et al.*, 2004, 2005; Molina *et al.*, 2009; Beard, 2019).

Incongruent melting of olivine

In Ol-metagabbros (Figs. 9a-b), coronas of tabular and columnar orthopyroxene grains, with a composition similar to that from granoblastic aggregates (Al = 0.073–0.15 apfu, Ca = 0.007–0.024

apfu, and Mg/(Mg + Fe^{2+}) = 0.66–0.83; Figs. 7a and c), appear around olivine (Fo$_{63–83}$; Fo = 100∗Mg/(Mg + Fe^{2+}) atomic ratio).

The coronas are mostly developed at the grain boundaries between olivine and plagioclase (Fig. 9a). The interface between olivine and orthopyroxene is convex towards olivine, being consistent with the partial dissolution of the former (c.f., Joesten, 1986). By contrast, the orthopyroxene-plagioclase interface can be flat or slightly curved whereas the polysynthetic twinning of plagioclase grains is not truncated by the grain boundary (Fig. 9a). These textural relationships suggest that plagioclase was not involved in the replacement of olivine by orthopyroxene. The coronas can also appear at olivine-pargasite interfaces (Fig. 9b), but locally these mineral phases can be in direct contact, thus suggesting that they were not unstable.

There has been a great deal of debate about the origin of orthopyroxene coronas, with both igneous and metamorphic origins being proposed (see detailed revisions in Joesten, 1986; De Haas *et al.,* 2002; Gallien *et al.,* 2012), but the textural relationships of the EASMC Ol-metagabbros (c.f., Fig. 2b in Beard, 2019) are more consistent with the reaction of olivine with melt without any involvement of plagioclase or pargasite:

$$Ol + SiO_2 (\text{in melt}) \rightarrow Opx$$
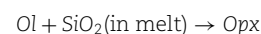
This mechanism also resolves the excess of Al, Ca and Na, and of Ti, Al, Ca, Na, K, and H_2O that would have been produced if plagioclase or pargasite, respectively, were involved in the reaction. This replacement corresponds to the classical peritectic dissolution reaction of olivine prescribed by the Bowen's discontinuous
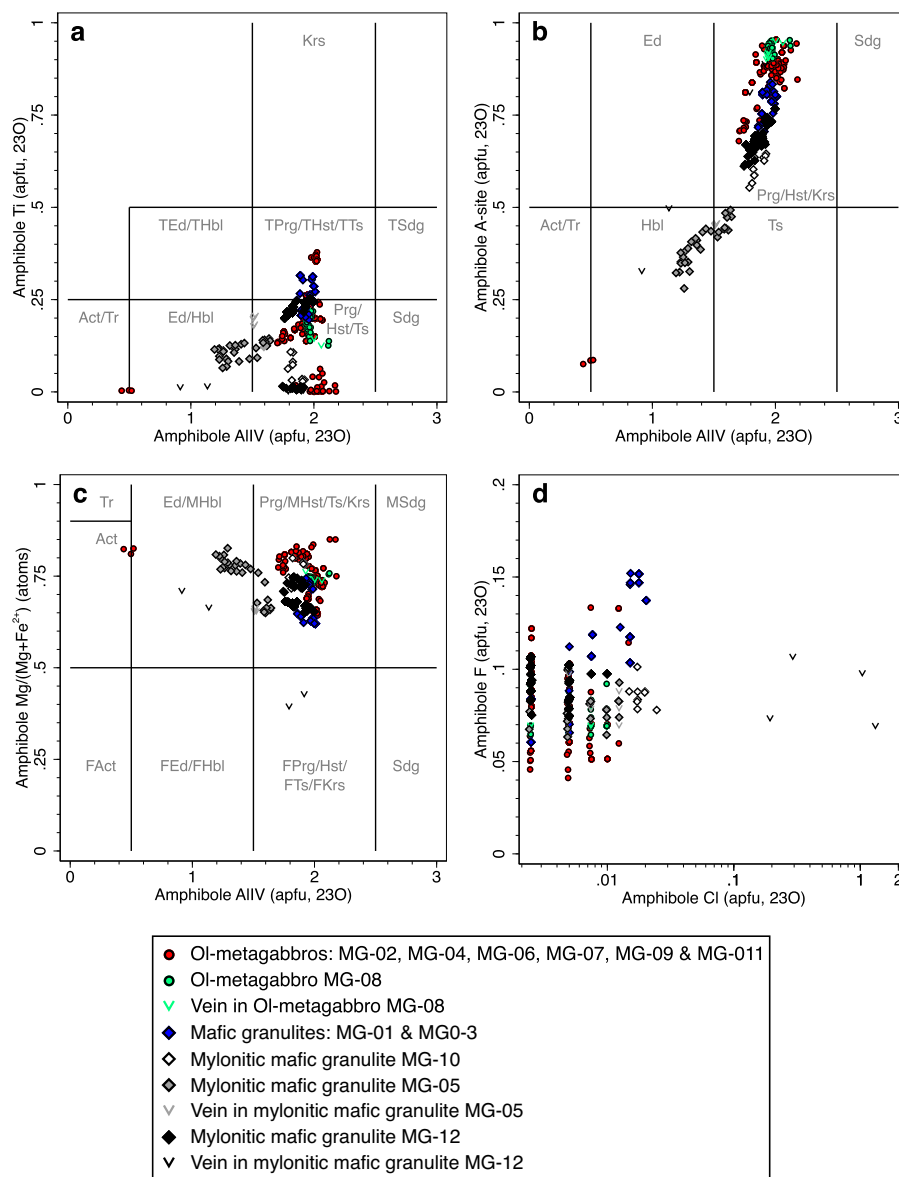
Fig. 5. Amphibole composition in high-grade mafic rocks from the Eastern Adrar–Suttuf Metamafic Complex. (a) Ti versus AlIV occupancies. (b) A-site versus AlIV occupancies. (c) Mg/(Mg + Fe^{2+}) ratio versus AlIV occupancy. (d) Cl versus F occupancies.

reaction series (Bowen, 1922) and is consistent with the tholeiitic character of the magmatism.

An-rich spikes: Evidence for the action of hydrous melts

In most samples of Ol-metagabbros and mafic granulites, An-rich spikes can appear at the rims of plagioclase grains from the granoblastic aggregates, achieving An$_{66–75}$ in MG-09, An$_{70–78}$ in MG-01, An$_{75–77}$ in MG-02, An$_{80–87}$ in MG-03 and An$_{87–92}$ in MG-07 (e.g. Figs. 4c from Ol-metagabbro MG-09, and 10c and 14a from mafic granulite MG-03).

This textural feature has been considered as an indication for (i) infiltration of a reactive hydrous mobile phase in gabbroic rocks, being proposed either a melt (e.g. Koepke *et al., 2005a*, 2005b, 2014) or a fluid (e.g. Bosch *et al., 2004*; Maier *et al., 2021*), or, conversely, for (ii) crystallisation from an in situ hydrous residual melt (e.g. Müller *et al., 2022*). In the EASMC high-grade mafic rocks, the near-solidus conditions estimated for textural maturation (see next section) suggest that it is more likely the involvement of an in situ hydrous residual melt.

Dolomite recrystallisation during textural maturation

Dolomite (Ca = 0.50–0.51 apfu (3 O) and Mg/(Mg + Fe^{2+}) = 0.84–0.93) is ubiquitous in Ol-metagabbros and mafic granulites. This mineral phase can occur within the rock matrix jointly with various combinations of clinopyroxene, orthopyroxene, pargasite, plagioclase, spinel, and magnetite (Figs. 10a-c). It also appears, along with clinopyroxene and orthopyroxene, entrapped in anhedral cores of bytownite replaced by labradorite (Fig. 10d). The interfaces between dolomite and silicate minerals present diverse degrees of textural maturation, appearing rounded shapes that suggest recrystallisation at high-temperature conditions (compare Figs. 10b and d), i.e. during the magmatic to metamorphic transition.

Pargasite veins crosscutting granoblastic aggregates as evidence for melt-assisted segregation

The pargasite from veins crosscutting the layering of Ol-metagabbros displays a granoblastic texture similar to that of the host-rock matrix (Figs. 11a-b), indicating that textural maturation
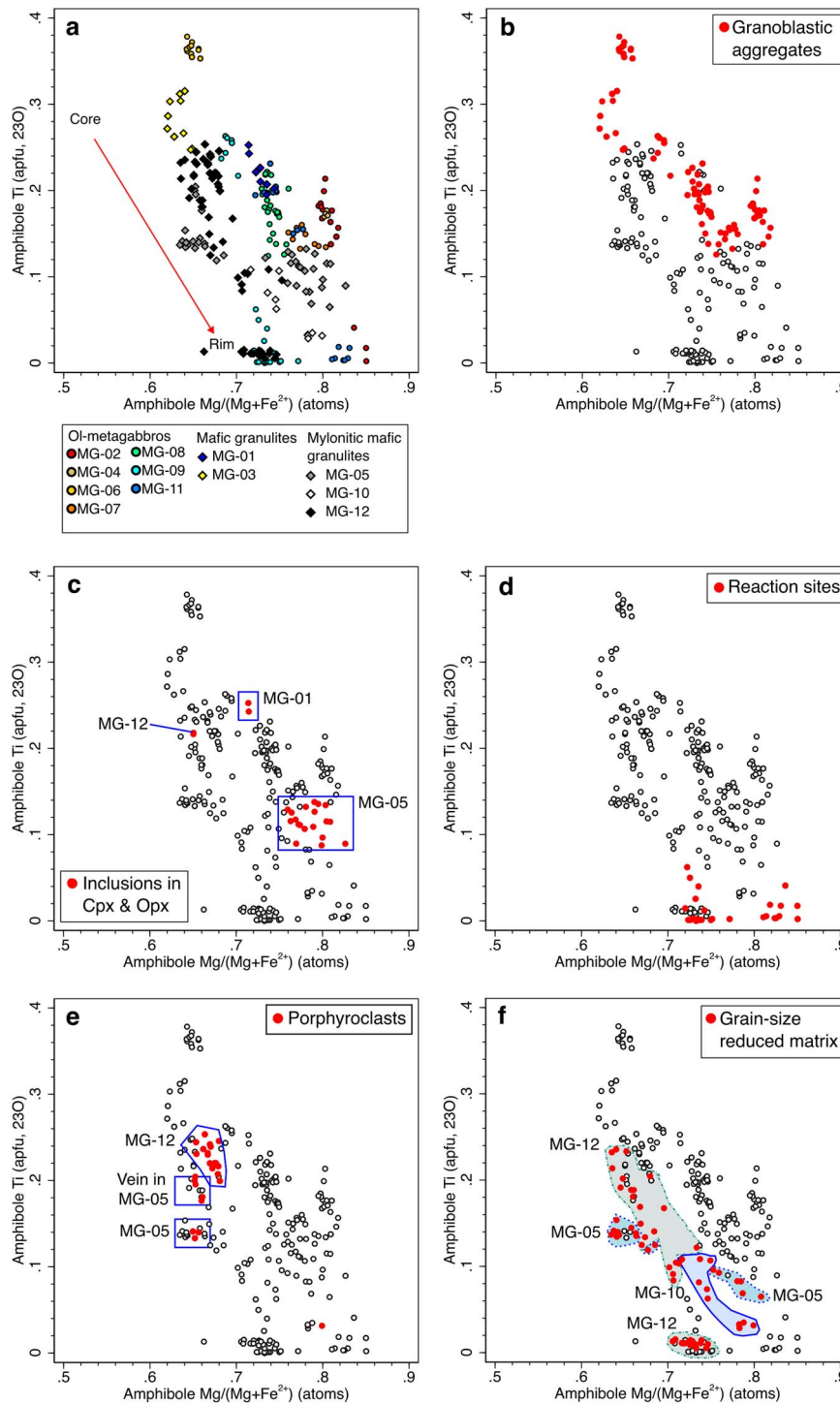
Fig. 6. Ti occupancy versus Mg/(Mg + Fe^{2+}) ratio in amphibole from high-grade mafic rocks from the Eastern Adrar–Suttuf Metamafic Complex. (a) Composition of amphibole displayed by samples. (b) Composition of amphibole from granoblastic aggregates. (c) Composition of amphibole included in resorbed grains of clinopyroxene and orthopyroxene. (d) Composition of amphibole at reaction sites. (e) Composition of amphibole porphyroclasts. (f) Composition of amphibole from grain-size reduced polycrystalline matrix.

due to annealing took place after the formation of pargasite veins. Its composition is also similar to that of the granoblastic aggregates (Figs. 5a-c; sample MG-08). Notably, the selvages of the veins are depleted in pargasite, suggesting local segregation of this mineral phase into the vein.

The evidence for interstitial melts during textural maturation previously discussed suggests that this segregation could most likely have been mediated by a melt.

Fluid-mediated reaction processes during cooling

A large variety of tiny symplectitic aggregates, i.e. vermicular intergrowths of two or more minerals (e.g. Keevil *et al.,* 2020), were produced upon cooling at reaction sites located along the grain boundaries of the granoblastic aggregates from the EASMC high-grade mafic rocks (Figs. 10, 12-14).

The origin of symplectites has been intensely debated (e.g. see Spruzeniece *et al.,* 2017, for a review). Hydrothermal
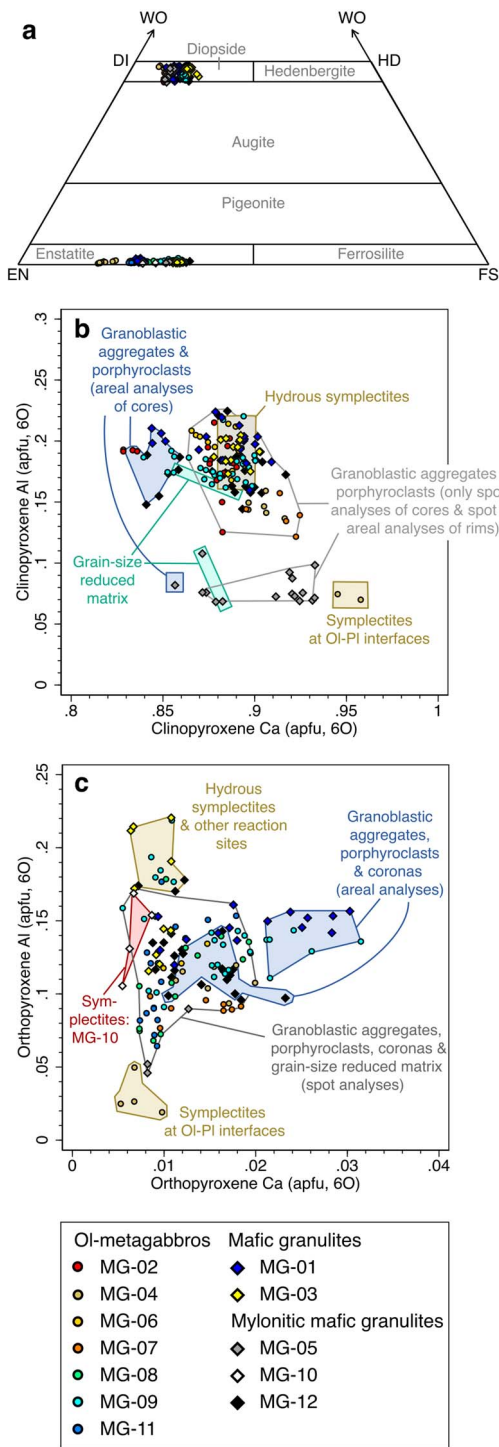
Fig. 7. Pyroxene composition in high-grade mafic rocks from the Eastern Adrar–Suttuf Metamafic Complex. (a) Wo–En–Fs classification diagram. (b) Ca versus Al occupancies in clinopyroxene. (c) Ca versus Al occupancies in orthopyroxene.

Fig. 8. Mineral compositional relationships in high-grade mafic rocks from the Eastern Adrar–Suttuf Metamafic Complex. (a) $100*Cr/(Cr+Al)$ versus $100*Fe^{2+}/(Mg+Fe^{2+})$ classification diagram for spinel-group minerals. (b) Fe^{3+}–Al–Cr classification diagram for spinel-group minerals. Spinel compositional fields from Barnes & Roeder (2001). (c) Rt–Hem–Wus classification diagram for Fe–Ti oxides.

experiments conducted by Spruzeniece et al. (2017) have demonstrated the importance of dissolution–precipitation mechanisms in the growth of symplectites. This process results in the creation of micropores that are filled by fluids or melts at the time of reaction, thus proving to be very useful for textural interpretation (c.f., Putnis, 2002, 2009), as previously indicated.

The EASMC high-grade mafic rocks contain both hydrous and anhydrous symplectites. They are characterised, as shown
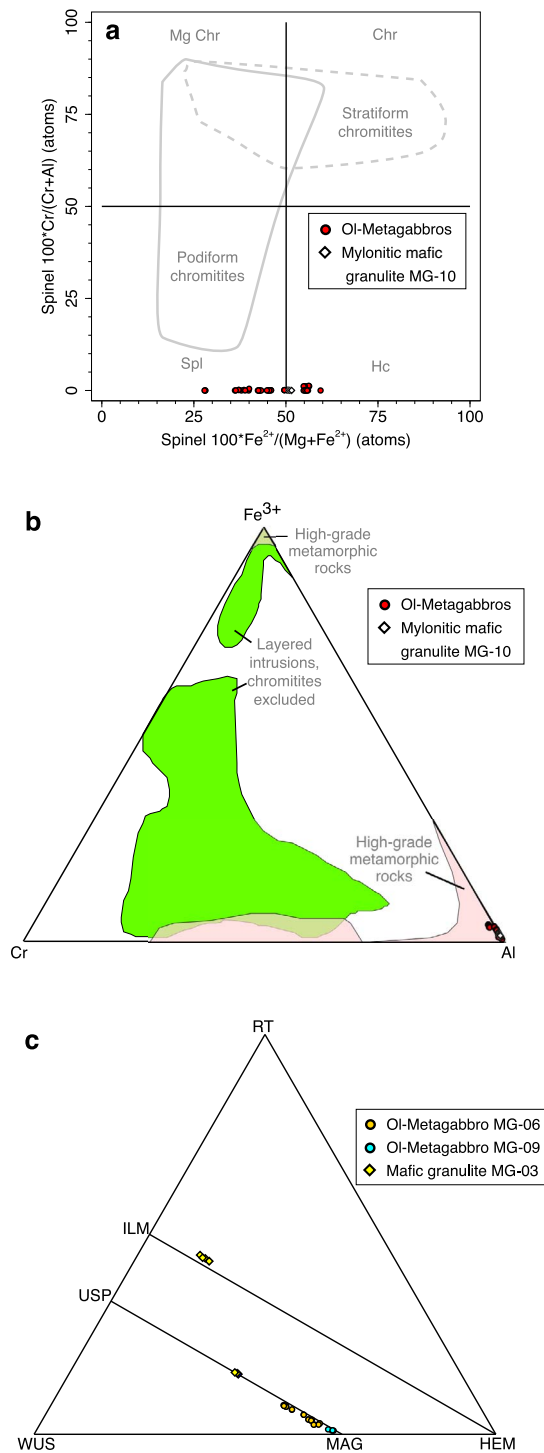
below, by the development of micropores in the mineral reaction products, thus attesting to the involvement of fluids in the replacements.

Anhydrous symplectites

In Ol-metagabbros, there are anhydrous symplectites of clinopyroxene, orthopyroxene, and spinel at olivine-plagioclase grain
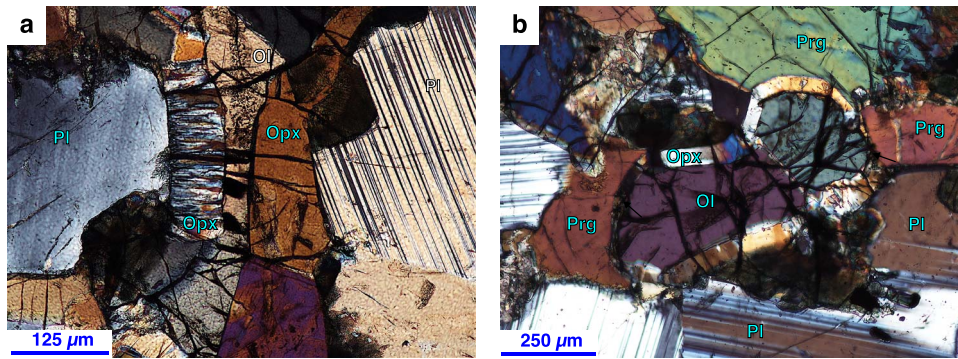
Fig. 9. Microphotographs of olivine textural relationships in Ol-metagabbro MG-08 from the Eastern Adrar–Suttuf Metamafic Complex. (a) Microphotograph of a corona of columnar and tabular orthopyroxene at the grain boundaries between olivine and plagioclase. Cross-polarised light. (b) Microphotograph of orthopyroxene corona between the grain boundaries of olivine and pargasite. Note that olivine can be locally in contact with pargasite, thus suggesting equilibrium. Cross-polarised light. Mineral abbreviations after Whitney & Evans (2010).
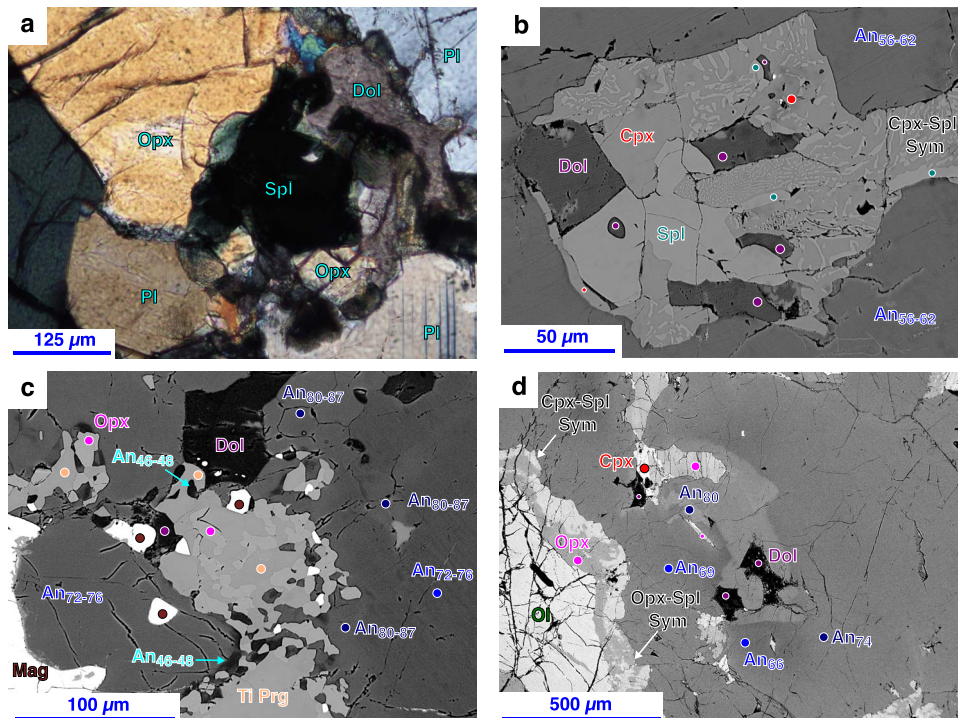

Fig. 10. Microphotographs and BSE images of dolomite textural relationships in Ol-metagabbros and mafic granulites from the Eastern Adrar–Suttuf Metamafic Complex. (a) Microphotograph of a tiny intergrowth of dolomite, spinel, orthopyroxene, and plagioclase in the rock matrix of Ol-metagabbro MG-08. Note that some interfaces at two-grain junctions are curved, whereas others are planar. Cross-polarised light. (b) BSE image of a tiny aggregate of clinopyroxene, spinel and dolomite, and very tiny symplectitic aggregates of clinopyroxene + spinel set in the interstices of an aggregate of labradorite from Ol-metagabbro MG-08. Note the occurrence of (i) one rounded inclusion of dolomite in spinel, (ii) planar to slightly curved interfaces at dolomite-clinopyroxene and dolomite-spinel junctions, (iii) laths of spinel and clinopyroxene along the grain boundaries of plagioclase with spinel, dolomite and symplectite and (iv) one tiny grain of dolomite within the symplectite that may be a relict of matrix dolomite. (c) BSE image of a medium-grained aggregate of bytownite, Ti pargasite, dolomite, and magnetite and fine-grained aggregate of anhedral orthopyroxene, Ti pargasite, andesine, magnetite, and dolomite in mafic granulite MG-03. Note An-rich spikes at plagioclase grain rims and planar to slightly curved grain boundaries of dolomite. (d) BSE image of anhedral grain core of bytownite replaced by labradorite with inclusions of dolomite, clinopyroxene and orthopyroxene with curved interfaces in Ol-metagabbro MG-04. Note a double corona between olivine and plagioclase with an inner shell of orthopyroxene and an outer shell of clinopyroxene-spinel and orthopyroxene-spinel symplectites (see close-up of symplectites in Fig. 12a). In BSE images, the colour of circles corresponds to the mineral indicated by the label with the same colour. Mineral abbreviations after Whitney & Evans (2010).

boundaries (Figs. 10d and 12a). Contrasting with the orthopyroxene coronas previously described, the interface between plagioclase and symplectite is much more complex (Fig. 10d), suggesting a reaction involving the consumption of plagioclase such as:

$$Ol + Pl \rightarrow Cpx + Opx + Spl$$
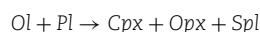
The compositions of clinopyroxene and orthopyroxene are characterized by significantly lower Al occupancies than those from the granoblastic aggregates (ranges: 0.069–0.075 apfu in clinopyroxene and 0.019–0.050 apfu in orthopyroxene; Figs. 7b-c). The composition of spinel is rich in Al (range: 1.91–1.93 apfu) with $Mg/(Mg + Fe^{2+})$ of ca. 0.71.

In these rock types, there are also orthopyroxene-magnetite symplectites (Fig. 12b) that may have been formed by oxidation of olivine at subsolidus or supersolidus conditions (c.f., Keevil et al., 2020; Wang et al., 2022).

In mafic granulites, anhydrous symplectites consist of quartz and aluminosilicate (Als, Al_2SiO_5 polymorph;
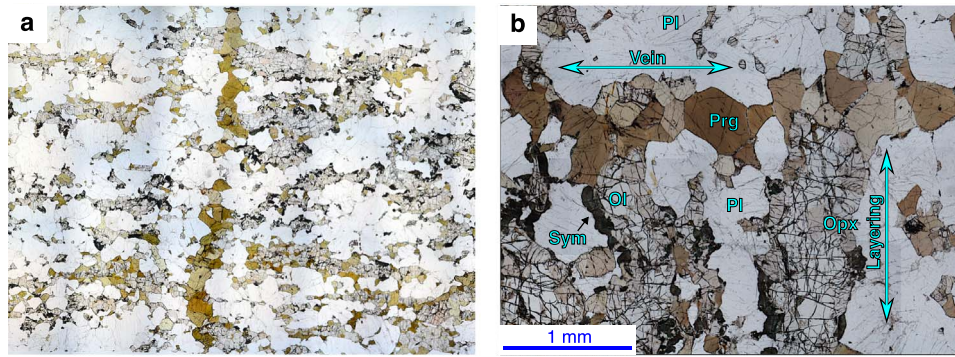
Fig. 11. Microphotographs of textural relationships of parasite veins in Ol-metagabbros from the Eastern Adrar–Suttuf Metamafic Complex. (a) Scanned digital image of a standard-size petrographic thin section of Ol-metagabbro MG-08 with one pargasite vein crosscutting a millimetre-scale layering defined by felsic and mafic minerals. Note depletion in pargasite at vein selvages. The thickness of the vein is ca. 1 mm. Plane-polarised light. (b) Close-up of the pargasite vein showing a granoblastic texture similar to that of the host-rock matrix. Plane-polarised light. Mineral abbreviations after Whitney & Evans (2010).
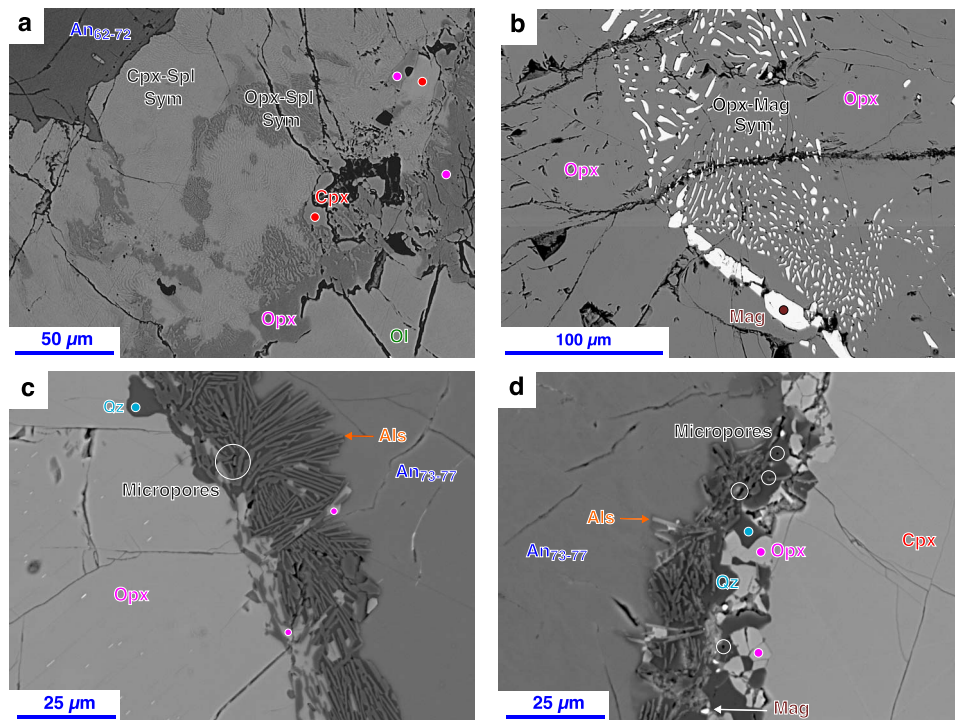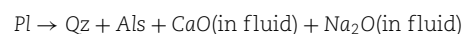

Fig. 12. BSE images of anhydrous symplectites in Ol-metagabbros and mafic granulites from the Eastern Adrar–Suttuf Metamafic Complex. (a) Close-up of the double corona between olivine and plagioclase from Fig. 10d (Ol-metagabbro MG-04). Note an inner shell of orthopyroxene and an outer shell of orthopyroxene-spinel and clinopyroxene-spinel symplectites. (b) Tiny symplectite aggregate of orthopyroxene and magnetite, probably after olivine, in Ol-metagabbro MG-09. Note a band of magnetite at the contact between the symplectitic aggregate and orthopyroxene. (c) Very tiny symplectitic aggregate of quartz and aluminosilicate at a bytownite-orthopyroxene grain boundary in mafic granulite MG-03. Note micropores with rounded shapes, some of them highlighted by white circles, microcracks filled with quartz along the grain boundary of orthopyroxene, and fan-shaped aluminosilicate needles that open towards plagioclase. The aluminosilicate shows acicular habit suggesting that it can be sillimanite. (d) Very tiny symplectitic aggregate of quartz, aluminosilicate, orthopyroxene, and magnetite at a bytownite-clinopyroxene grain boundary in mafic granulite MG-03. Note micropores with rounded shapes (some of them highlighted by white circles). The colour of circles corresponds to the mineral indicated by the label with the same colour. Mineral abbreviations after Whitney & Evans (2010).

Whitney & Evans, 2010) at bytownite-orthopyroxene grain boundaries (Fig. 12c), and quartz, aluminosilicate, orthopyroxene, and magnetite at bytownite-clinopyroxene grain boundaries (Fig. 12d). The aluminosilicate exhibits an acicular habit and is, therefore, most likely sillimanite, a mineral whose stability field is consistent with the P–T conditions estimated in the next section. The quartz-aluminosilicate aggregates display a fan-shaped opening towards plagioclase grains, thus suggesting the dissolution of plagioclase. These aggregates present rounded micropores that are consistent with the replacement being produced by a dissolution-precipitation mechanism assisted by fluids (c.f., Putnis, 2002, 2009; Putnis & Austrheim, 2013). Thus, these fluids could have transported the excess of CaO and Na$_2$O produced by the replacement according to the following open-system reaction:

$$Pl \rightarrow Qz + Als + CaO(\text{in fluid}) + Na_2O(\text{in fluid})$$

Hydrous symplectites

In Ol-metagabbros, there are hydrous symplectites of low-Ti pargasite, spinel, and andesine at the grain boundaries of plagioclase
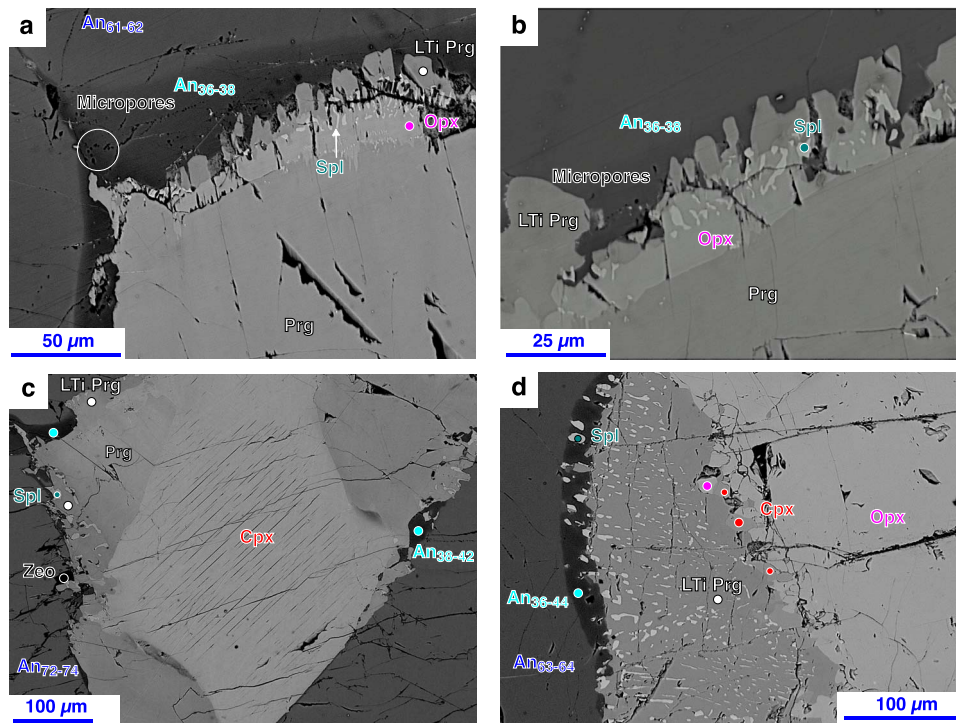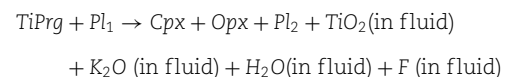
Fig. 13. BSE images of hydrous symplectites in Ol-metagabbros from the Eastern Adrar–Suttuf Metamafic Complex. (a) Double symplectite layer between pargasite and labradorite with one band of orthopyroxene and spinel, and another of low-Ti pargasite and andesine in sample MG-08. Note the appearance of (i) spinel limited to the orthopyroxene band, (ii) laths of low-Ti pargasite protruding into the plagioclase, (iii) replacement of pargasite by orthopyroxene at a very local scale and (iv) micropores with rounded shapes, some of them highlighted by white circles. (b) Detail of micropores at a reaction site in sample MG-08. (c) Low-Ti pargasite–spinel–andesine symplectite at the grain boundaries between zoned pargasite, clinopyroxene and labradorite in sample MG-02. Note the resorption of labradorite and clinopyroxene (only at a local scale) by the symplectite and the presence of spinel at the rim of andesine developed at the grain boundary between labradorite and pargasite. (d) Multiple symplectite layers between orthopyroxene and labradorite in sample MG-09, consisting of (i) a discontinuous band of tiny clinopyroxene at the orthopyroxene grain boundary showing evidence of corrosion, (ii) a thin band of andesine, low-Ti pargasite, and spinel at the labradorite grain boundary, and (iii) two bands between them, one of low-Ti pargasite and another of low-Ti pargasite and spinel. Note protrusion of low-Ti pargasite into the orthopyroxene, and of low-Ti pargasite + spinel into the plagioclase. The colour of circles corresponds to the mineral indicated by the label with the same colour. Mineral abbreviations after Whitney & Evans (2010).

with pargasite (Figs. 13a-b), clinopyroxene (Fig. 13c) and orthopyroxene (Fig. 13d), indicating the more general consumption of an infiltrated hydrous mobile phase during the cooling history of these rocks. The composition of amphibole is low-Ti pargasite (< 0.062 apfu Ti) with 0.85–2.18 apfu Al and $Mg/(Mg+Fe^{2+})$ of 0.72–0.85 (Figs. 5a-c, and 6d). Plagioclase composition is andesine with An_{36-47}. The composition of clinopyroxene is similar to that of spot analyses of cores and rims of grains from granoblastic aggregates (ranges: $Ca = 0.88$–0.90 apfu and $Al = 0.16$–0.22 apfu), but that of orthopyroxene shows a distinctive higher Al occupancy (range: 0.15–0.22 apfu) (Fig. 7). The composition of spinel from these symplectites is rich in Al (range: 1.90–1.95 apfu) with variable $Mg/(Mg+Fe^{2+})$ ratios that depend of the rock sample (ranges: MG-02: 0.59–0.62; MG-08: 0.55–0.56; MG-09: 0.40–0.44). Plagioclase, generally bytownite or labradorite, is replaced by andesine. Thus, the protrusion of laths of low-Ti pargasite and spinel into the plagioclase suggests the progress of this reaction band towards plagioclase (Fig. 13). Indeed, this process should have also been controlled by a dissolution-precipitation mechanism, as evidenced by the presence of micropores in the reaction band minerals.

In mafic granulite MG-03, it is remarkably the appearance of symplectites consisting of clinopyroxene, orthopyroxene, plagioclase, and magnetite replacing the rims of Ti pargasite grains (Figs. 14a-b). The compositions of clinopyroxene, orthopyroxene and plagioclase are similar to those previously reported

for hydrous symplectites from Ol-metagabbros (compositional ranges: 0.17–0.19 apfu Al and 0.88–0.90 apfu Ca in clinopyroxene; 0.19–0.22 apfu Al and 0.006–0.011 apfu Ca in orthopyroxene; An_{44-48} in plagioclase). A rim of andesine appears at the boundary between plagioclase from the rock matrix and the symplectite (Fig. 14b). There are micropores dispersed along these aggregates as well as tiny interstitial quartz at irregular, serrated, grain boundaries of pyroxenes (Figs. 14b-c) that suggest the presence of a reactive interstitial fluid phase that could account for an imbalance for TiO_2 that occurred during the replacement of Ti pargasite, as evidenced by the scarcity of Ti mineral phases in the symplectitic aggregate. Thus, the infiltration of an H_2O-rich fluid could explain the loss from the reaction site of TiO_2 and other components like K_2O and F, which are relatively abundant in Ti pargasite (compositional ranges: 0.25–0.31 apfu Ti, 0.19–0.25 apfu K, and 0.10–0.15 apfu F), implying an open system reaction as follows:

$$TiPrg + Pl_1 \rightarrow Cpx + Opx + Pl_2 + TiO_2 (\text{in fluid})$$
$$+ K_2O \ (\text{in fluid}) + H_2O(\text{in fluid}) + F \ (\text{in fluid})$$

This sample also exhibits a widespread growth of tiny grains of clinopyroxene and orthopyroxene at the interface of plagioclase with coarser grains of the same mineral phases (Figs. 12c-d and 14a), which complicates the understanding of
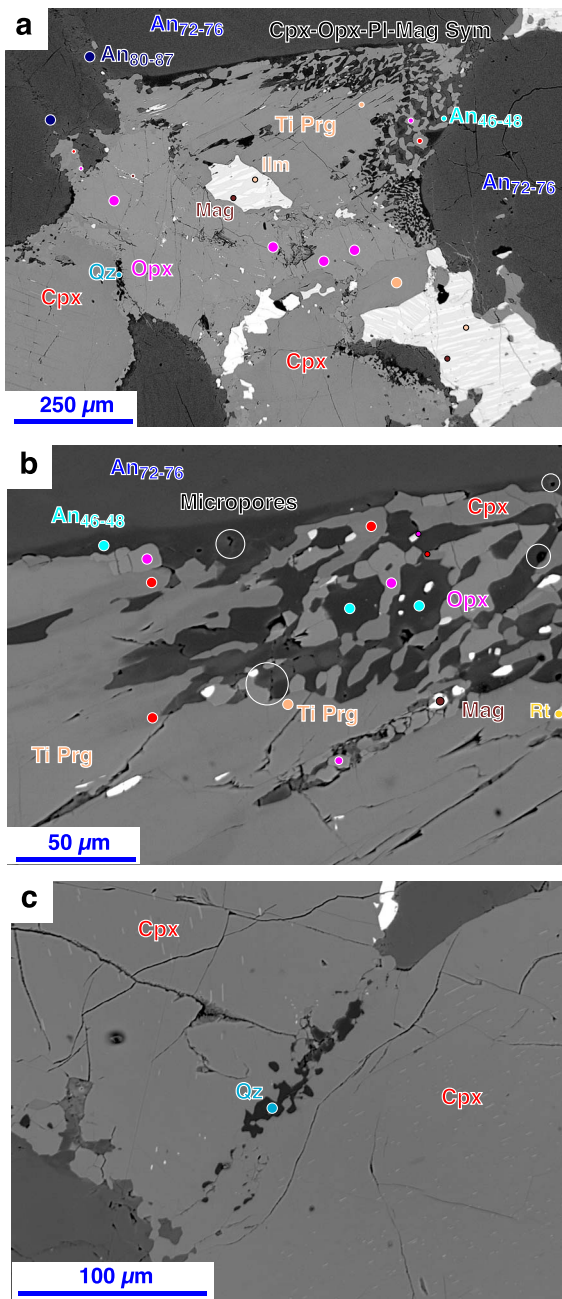
Fig. 14. BSE images of Ti pargasite replacement textures in mafic granulite MG-03 from the Eastern Adrar–Suttuf Metamafic Complex. (a) Medium-grained aggregate of clinopyroxene, orthopyroxene, Ti pargasite, labradorite and Fe–Ti oxides showing Ti pargasite replacement by a tiny aggregate of clinopyroxene, orthopyroxene, and andesine at grain rims and fractures. Note very tiny interstitial quartz at clinopyroxene-orthopyroxene grain boundaries and An-rich spikes at plagioclase grain rims. (b) Close-up of the Ti pargasite breakdown reaction texture. Note the presence of micropores with rounded shapes (some of them highlighted by white circles) and the scarcity of Ti minerals (only one tiny grain of rutile) in the reaction zone. (c) Close-up of very tiny interstitial quartz at the boundary of two clinopyroxene grains. Note clinopyroxene with an irregular, serrated, grain boundary with embayments filled by quartz. The colour of circles corresponds to the mineral indicated by the label with the same colour. Mineral abbreviations after Whitney & Evans (2010).

the mechanisms behind the development of the granoblastic texture. Nonetheless, it is remarkable to note that these relationships suggest that the formation of the pyroxene aggregates was

not driven by an intrinsic instability of Ti pargasite. Instead, their growth is more likely attributed to the action of the reactive fluids.

Mylonitic mafic granulites: Evidence of shearing during cooling

Mylonitic mafic granulites exposed in the border of the high-grade mafic bodies show porphyroclasts of amphibole, clinopyroxene, orthopyroxene, and plagioclase with undulose extinction, mechanical twinning and bending that are set in a grain-size reduced polycrystalline matrix (Figs. 15a-d). Remarkably, it appears amphibole-spinel and orthopyroxene symplectites with undulose extinction in sample MG-10 (Figs. 15e-f), thus evidencing that shearing took place after symplectite generation.

Amphibole composition is very variable (Figs. 5a-c, and 6e-f). In sample MG-05, the composition of amphibole porphyroclasts is tschermakite with 0.13–0.14 apfu Ti, 1.58–1.60 apfu AlIV, ca. 0.44 apfu A-site and $Mg/(Mg + Fe^{2+})$ of 0.65–0.66; amphibole from the transposed veins is also tschermakite, but with slightly lower AlIV and higher Ti occupancies (ranges: 1.51–1.52 apfu and 0.18–0.20 apfu, respectively). In this rock type, it appears amphibole included in clinopyroxene and orthopyroxene with hornblende composition (Ti = 0.088–0.13 apfu, AlIV = 1.19–1.48 apfu, A-site = 0.32–0.44 apfu, and $Mg/(Mg + Fe^{2+})$ = 0.78–0.83). In sample MG-12, the composition of amphibole porphyroclasts is Ti pargasite with 0.20–0.25 apfu Ti, 1.76–2.00 apfu AlIV, 0.62–0.77 apfu A-site, and $Mg/(Mg + Fe^{2+})$ of 0.65–0.68. The composition of amphibole from the rock matrix of both samples is very variable, achieving lower Ti occupancies (ranges: 0.065–0.14 apfu in MG-05 and 0.006–0.24 apfu in MG-12). In sample MG-10, amphibole from the rock matrix and symplectites has low-Ti pargasite composition (Ti = 0.028–0.10 apfu). The composition of *plagioclase* from porphyroclasts is labradorite–bytownite (An$_{79-87}$ in MG-05, An$_{83-84}$ in MG-10, and An$_{70-85}$ in MG-12); this from the rock matrix is much variable, ranging from andesine to anorthite (An$_{82-89}$ in MG-05, An$_{84-92}$ in MG-10, and An$_{56-84}$ in MG-12). The more calcic compositions from the rock matrix witness the milling and grinding of pre-existing plagioclase grains with An-rich spikes at their rims. On the other hand, the low-Ti pargasite (0.006–0.015 apfu Ti) and andesine (An$_{38-49}$) grains from the rock matrix of sample MG-12 could represent former reaction sites affected by mylonitisation. *Clinopyroxene* porphyroclasts from sample MG-12 present similar textural and compositional relationships to those from granoblastic aggregates (Figs. 7b and 15g), with reintegrated compositions of diopside with 0.15–0.19 apfu Al, 0.84–0.86 apfu Ca, CaTs$_{2-5}$, and $Mg/(Mg + Fe^{2+})$ of 0.78–0.81 in the cores, and 0.14–0.19 apfu Al, 0.88–0.90 apfu Ca, CaTs$_{2-5}$, and $Mg/(Mg + Fe^{2+})$ of 0.79–0.83 at the rims. Spot analyses of cores and rims of the porphyroclasts from this sample have Ca occupancies close to these latter (range: 0.88–0.92 apfu). Clinopyroxene porphyroclasts from sample MG-05, as happens with amphibole, show significantly lower Al occupancies (range: 0.068–0.098 apfu). The composition of matrix clinopyroxene has 0.86–0.89 apfu Ca with Al occupancy ranging 0.069–0.11 apfu in sample MG-05 and 0.16–0.18 apfu in sample MG-12. The *orthopyroxene* porphyroclasts show very tiny exsolution lamellae of clinopyroxene (Fig. 15h). They have reintegrated compositions of enstatite with slightly lower Ca occupancies than those from the granoblastic aggregates (range: 0.010–0.023 apfu; Fig. 7c) suggesting a more intense compositional resetting during mylonitisation. Their spot analyses tend to show lower Ca occupancy (<0.019 apfu). The composition of orthopyroxene from the rock matrix also shows low Ca occupancies (range: 0.008–0.013 apfu). Orthopyroxene from symplectites from sample
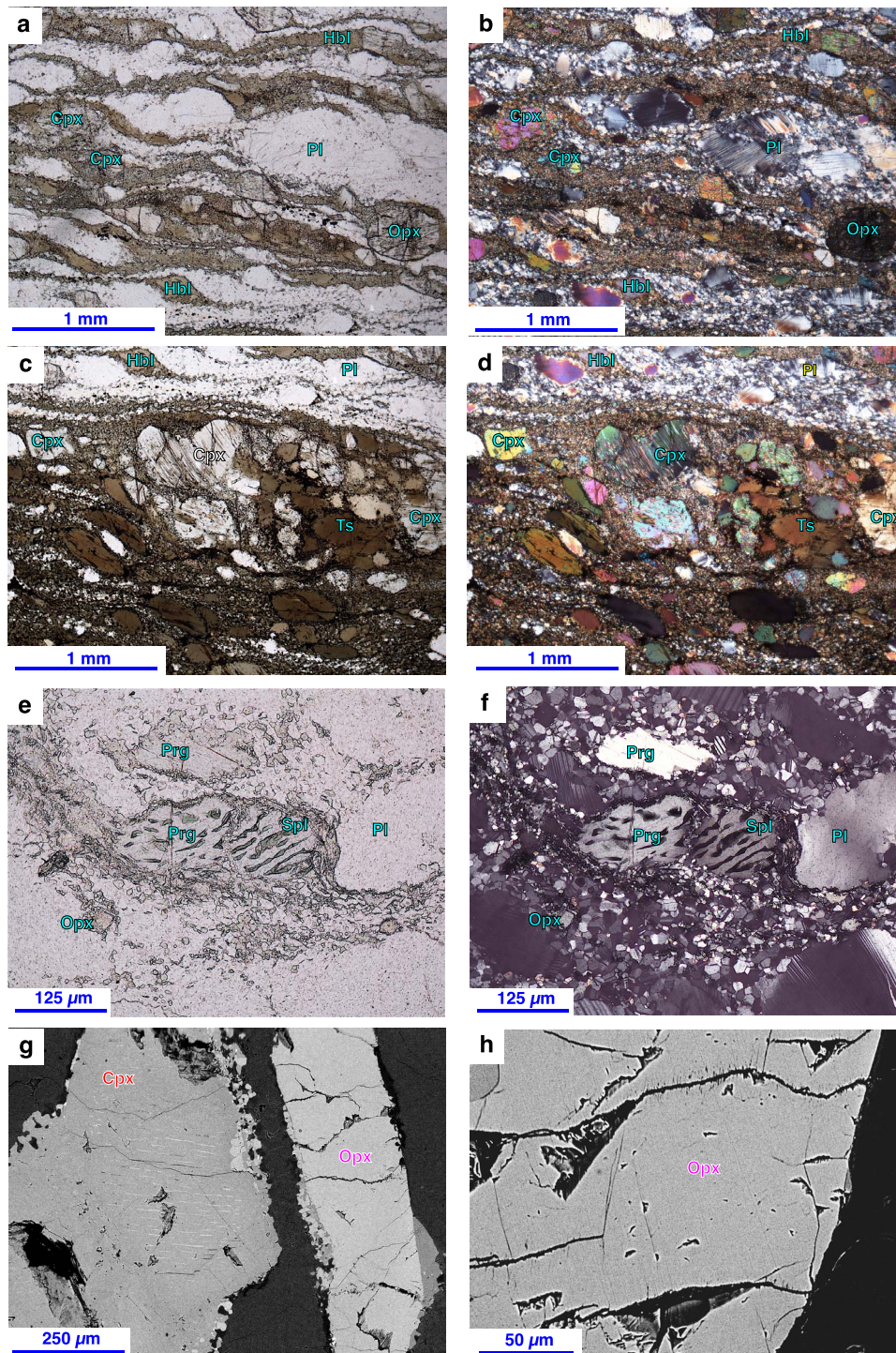
Fig. 15. Microphotographs and BSE images of mylonitic textures in high-grade mafic rocks from the Eastern Adrar–Suttuf Metamafic Complex. (a, plane-polarised light, and b, cross-polarised light) Porphyroclasts of clinopyroxene, orthopyroxene, hornblende and plagioclase developing undulose extinction, mechanical twinning and bending set in a grain-size reduced polycrystalline matrix from mylonitic mafic granulite MG-05. (c, plane-polarised light, and d, cross-polarised light) Detail of the contact between a transposed vein of tschermakite and the host rock in mylonitic mafic granulite MG-05. (e, plane-polarised light, and f, cross-polarised light) Porphyroclasts of relatively coarse pargasite–spinel symplectite, pargasite and plagioclase with undulose extinction set in a grain-size reduced polycrystalline matrix from mylonitic mafic granulite MG-10. (g) BSE image of clinopyroxene porphyroclast from mylonitic mafic granulite MG-12 exhibiting exsolution lamellae of orthopyroxene at its core. (h) BSE image of orthopyroxene porphyroclast from mylonitic mafic granulite MG-12 exhibiting very tiny exsolution lamellae of clinopyroxene. Mineral abbreviations after Whitney & Evans (2010).

MG-10 has a very low Ca occupancy (range: 0.005–0.009 apfu), whereas Al occupancy is relatively high (range: 0.11–0.17 apfu). The composition of *spinel* from symplectites shows the highest Al occupancies (range: 1.95–1.97 apfu).

Late veins: Evidence for fracture-focused fluid flow

The sheared mafic granulites present veins crosscutting the mylonitic banding, thus evidencing a late fracture-focused
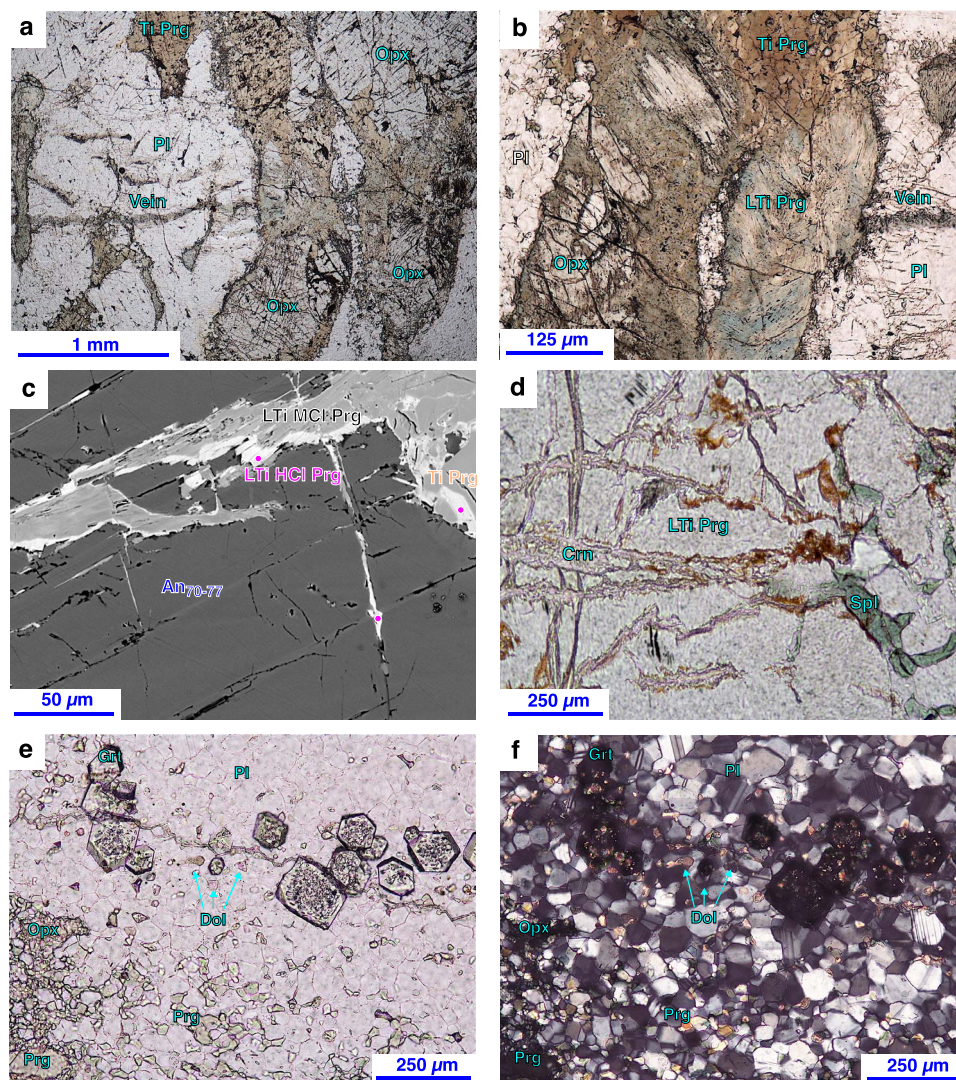
Fig. 16. Microphotographs and BSE images of later veins in high-grade mafic rocks from the Eastern Adrar–Suttuf Metamafic Complex. (a and b) Microphotographs of Cl-bearing pargasite veins crosscutting the mylonitic banding in mylonitic mafic granulite MG-12. Note the partial replacement of orthopyroxene by Cl-bearing pargasite and an aggregate of Cl-bearing pargasite that can probably be a pseudomorphic replacement of clinopyroxene. Plane-polarised light. (c) BSE image showing a close-up of the Cl-bearing pargasite vein from mylonitic mafic granulite MG-12. Note low-Ti, mid-Cl pargasite grains (ca. 0.3–0.4 apfu Cl) filling a vein crosscutting a plagioclase grain that are rimmed by low-Ti, high-Cl pargasite (up to ca. 1.3 apfu Cl). (d) Microphotograph of tiny veins filled with corundum in a porphyroclast of low-Ti pargasite–spinel symplectite from mylonitic mafic granulite MG-10. Plane-polarised light. (e, plane-polarised light, and f, cross-polarised light) Very tiny vein of dolomite crosscutting the grain-size reduced matrix of mylonitic mafic granulite MG-10. Note very tiny euhedral garnet grains with minute inclusions of dolomite occurring along the vein selvages. In BSE images, the colour of circles corresponds to the mineral indicated by the label with the same colour. Mineral abbreviations after Whitney & Evans (2010).

fluid flow after mylonitisation. Three different types of veins are distinguished: (i) Cl-bearing pargasite veins (0.19–1.32 apfu Cl; Figs. 5a-d and 16a-c), (ii) corundum veins (Fig. 16d) and (iii) dolomite veins (Figs. 16e-f).

Cl-bearing pargasite veins crosscut plagioclase and pyroxene grains from the rock matrix of sample MG-12; an intense alteration was produced in their selvages, appearing very tiny aggregates of secondary amphibole replacing pyroxene (Figs. 16a-b). Corundum and dolomite veins appear in sample MG-10 crosscutting, respectively, the strained low-Ti pargasite–spinel symplectites and the grain-size reduced matrix. The effects of vein fluids on the host rock are less intense than in the first type, being limited to the formation of very tiny euhedral grains of garnet (almandine with Gro_{16-20} and Prp_{32-40}, where $Gro = 100*Ca/(Ca + Mg + Fe^{2+} + Mn)$ and

$Prp = 100*Mg/(Ca + Mg + Fe^{2+} + Mn))$ along the selvages of the dolomite veins.

P–T ESTIMATIONS: A DECOMPRESSION-COOLING PATH FROM HT-UHT GRANULITE- TO AMPHIBOLITE-FACIES CONDITIONS

The texture relationships in the EASMC high-grade mafic rocks suggest *melt-mediated processes* during texture maturation of the rock matrix, incongruent dissolution melting of olivine and pyroxenes, generation of An-rich spikes and high-temperature veining, and *fluid-mediated processes* during symplectite growth at mineral grain boundaries upon cooling. In this section, the P–T conditions of the transition from a magmatic to metamorphic
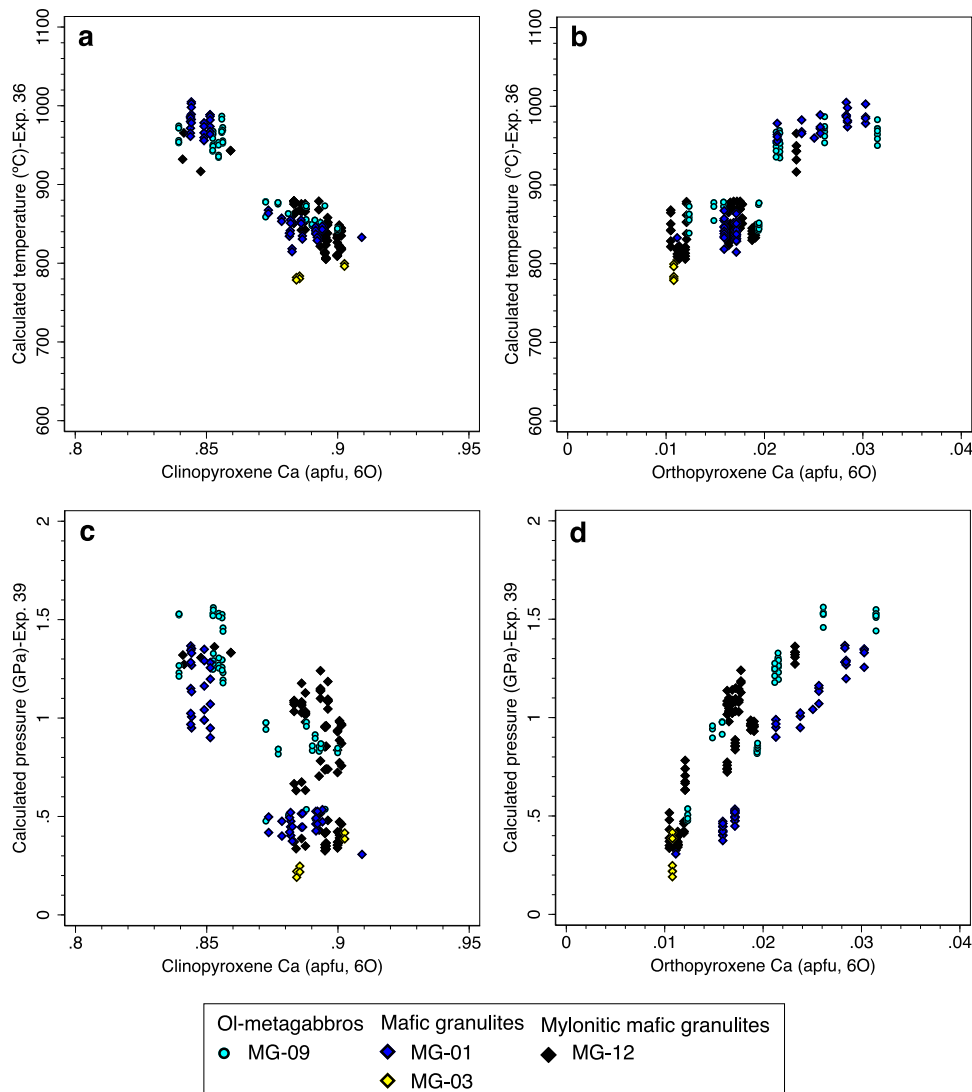
Fig. 17. Two-pyroxene thermobarometry in high-grade mafic rocks from the Eastern Adrar–Suttuf Metamafic Complex. (a) Temperatures given by two-pyroxene thermometry versus clinopyroxene Ca occupancy. (b) Temperatures given by two-pyroxene thermometry versus orthopyroxene Ca occupancy. (c) Pressures given by two-pyroxene barometry versus clinopyroxene Ca occupancy. (d) Pressures given by two-pyroxene barometry versus orthopyroxene Ca occupancy. P–T conditions determined using calibrations 36 and 39 from Putirka (2008).

environment and the late cooling are contrained using classical thermobarometry and calculations of phase stability diagrams. The equilibrium P–T conditions were determined using amphibole–plagioclase thermobarometry (Molina *et al.,* 2015, 2021), two-pyroxene thermobarometry (Putirka, 2008) and Ti-in-amphibole thermometry (Liao *et al., 2021*). The P–T stability fields determined for the mineral assemblages were tested by thermodynamic modelling using the GeoPS program (Xiang & Connolly, 2022).

Classical thermobarometry
Methods

The P–T conditions for clinopyroxene-orthopyroxene equilibration were calculated by two-pyroxene thermobarometry, using expressions 36 (based on the partitioning of enstatite + ferrosilite between clinopyroxene and orthopyroxene) and 39 (based on the method of Mercier *et al.,* 1984) from Putirka (2008), with precisions of, respectively, ±45°C (precision reported at 1 s level) and ±280 MPa for $Mg/(Mg+Fe^{2+})$ ratios in clinopyroxene >0.75. Temperature estimates for amphibole equilibration were computed by amphibole–plagioclase NaSi-CaAl exchange thermom-

etry, using the almost P-independent calibrations A1 and A2, and the P-independent calibration B2 of Molina *et al.* (2021) (precision: ±50°C), which give accurate results for Mg-rich amphiboles, and by Ti-in-amphibole thermometry, using the calibration of Liao *et al.* (2021) (precision: ±35°C) for subalkaline systems saturated in a Ti mineral phase (rutile, ilmenite, or titanite). Pressure estimates were calculated using the calibration of the amphibole–plagioclase Al-Si partitioning barometer of Molina *et al.* (2015) (precision: ±150–200 MPa) at the temperatures obtained by the thermometric expressions A1, A2 and B2.

It was selected four samples (Ol-metagabbro MG-09, mafic granulites MG-01 and MG-03, and mylonitic mafic granulite MG-12) for two-pyroxene thermobarometry and seven samples (Ol-metagabbros MG-08, MG-09, and MG-11, mafic granulites MG-01 and MG-03, and mylonitic mafic granulites MG-05 and MG-12) for amphibole–plagioclase thermobarometry.

Amphibole formulas were calculated assuming 13 cations exclusive of Ca, Na and K (13-CNK method; Robinson *et al.,* 1982) for the amphibole–plagioclase barometer and a modified version of the average Fe^{3+} method of Spear & Kimball (1984)
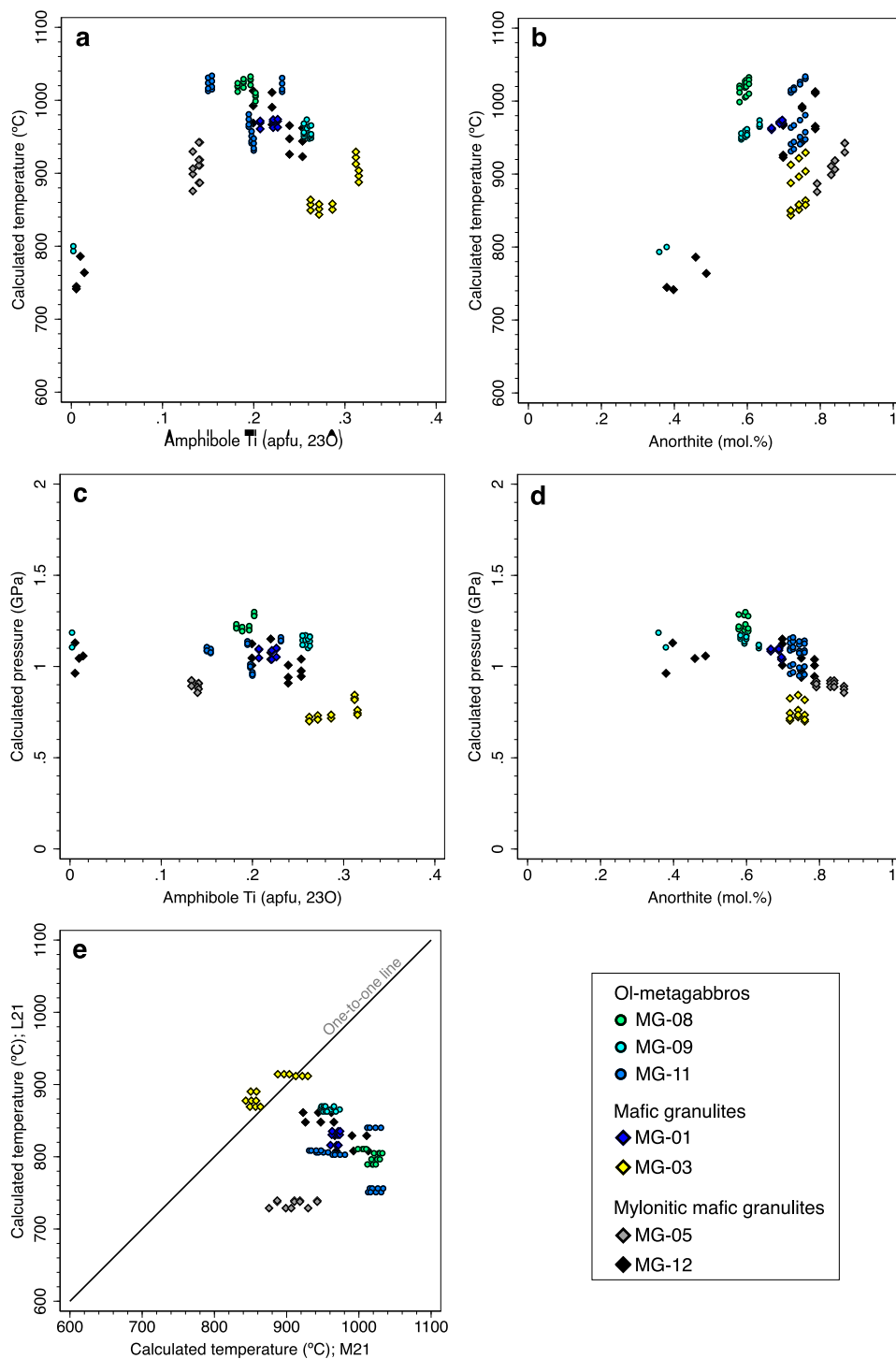
Fig. 18. Amphibole–plagioclase and Ti-in-amphibole thermobarometry in high-grade mafic rocks from the Eastern Adrar–Suttuf Metamafic Complex. (a) Temperatures given by amphibole–plagioclase thermometry versus amphibole Ti occupancy. (b) Temperatures given by amphibole–plagioclase thermometry versus anorthite content of plagioclase. (c) Pressures given by amphibole–plagioclase barometry versus amphibole Ti occupancy. (d) Pressures given by amphibole–plagioclase barometry versus anorthite content of plagioclase. (e) Relationships of temperatures given by amphibole–plagioclase and Ti-in-amphibole thermometry. Note the consistency of results for sample MG-03 that presents ilmenite in the rock matrix. P–T conditions determined using calibrations of the amphibole–plagioclase thermometer by Molina *et al.* (2021), the Ti-in-amphibole thermometer from Liao *et al.* (2021) and the amphibole–plagioclase barometer from Molina *et al.* (2015). Abbreviations: L21, temperatures given by the Ti-in-amphibole thermometer from Liao *et al.* (2021); M21, temperatures given by amphibole–plagioclase thermometers from Molina *et al.* (2021).

described in Dale *et al.* (2005) for the amphibole–plagioclase and the Ti-in-amphibole thermometers. For two-pyroxene thermobarometry, mineral formulas and parameters required for using the expressions were calculated following the procedure presented in Tables 2 and 3 by Putirka (2008).

The amphibole–plagioclase thermobarometric calculations were performed using paired rims of grains in mutual contact at reaction sites or, for grain cores, using different pairs that cover the compositional range of the two mineral phases in the samples. In the same way, reintegrated compositional pairs encompassing
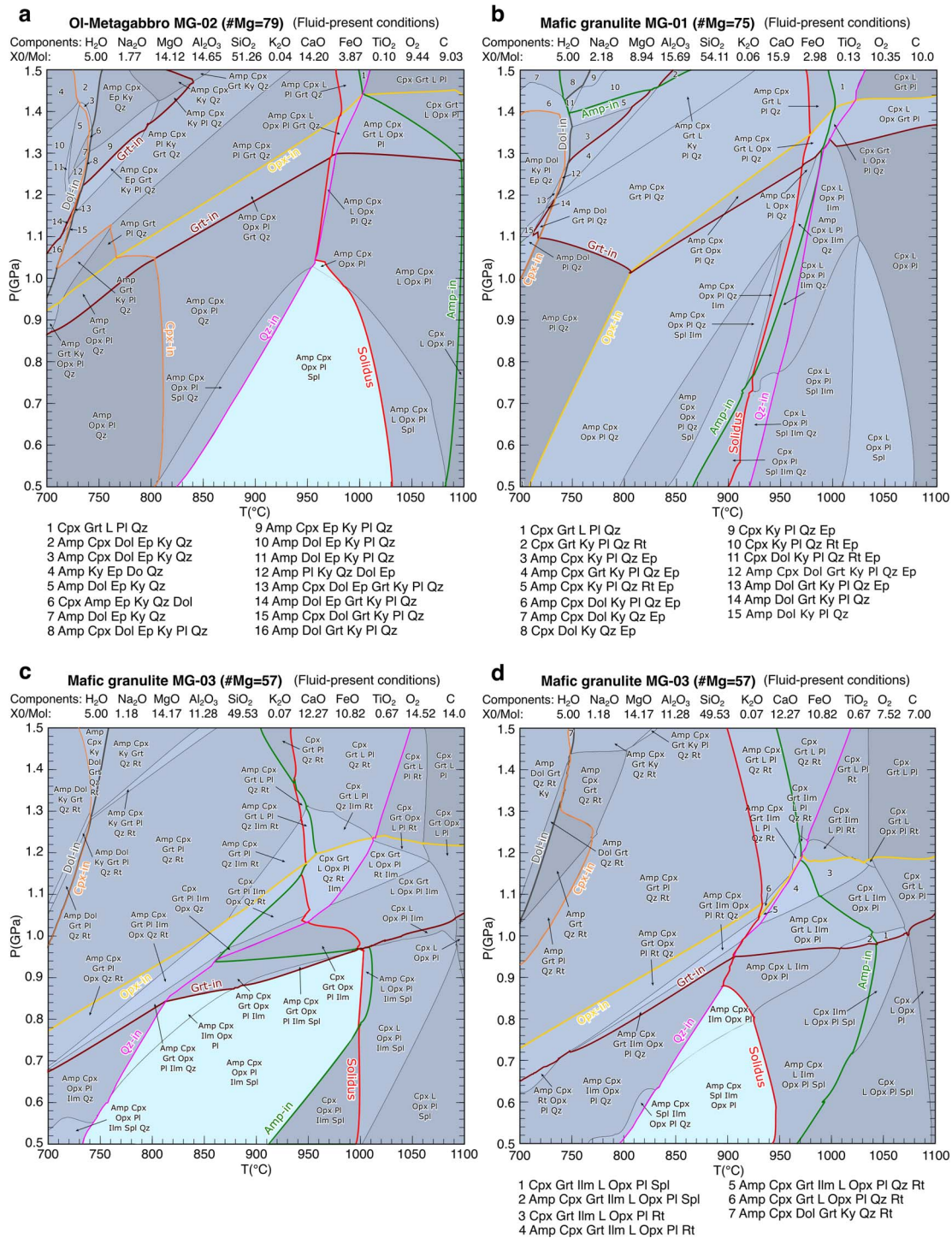
Fig. 19. Calculated P–T phase diagrams for high-grade mafic rocks from the Eastern Adrar–Suttuf Metamafic Complex. (a) Phase relations in Ol-metagabbro MG-02 with H_2O = 5 moles, O_2 = 9.44 moles, and C = 9.03 moles. (b) Phase relations in mafic granulite MG-01 with H_2O = 5 moles, O_2 = 10.35 moles, and C = 10 moles. (c) Phase relations in mafic granulite MG-03 with H_2O = 5 moles, O_2 = 14.52 moles, and C = 14 moles. (d) Phase relations in mafic granulite MG-03 with H_2O = 5 moles, O_2 = 7.52 moles, and C = 7 moles. Calculations performed with GeoPS program (Xiang & Connolly, 2022) using the internally consistent thermodynamic dataset of Holland & Powell (2011, updated version HP633) and the following mixing models: cAmph(G) for amphibole (Green *et al.*, 2016), Cpx(HGP) for clinopyroxene, Gt(HGP) for garnet, Melt(HGP) for silicate melt, O(HGP) for olivine, Opx(HGP) for orthopyroxene and Sp(HGP) for spinel-group minerals (Holland *et al.*, 2018), Ilm(W) for ilmenite (White *et al.*, 2014), Fsp(C1) for plagioclase (Holland & Powell, 2003), Ep(HP11) for epidote and F for H_2O–CO_2 fluids (Holland & Powell, 2011), and dis(EF) and oCcM(EF) for carbonates (Franzolin *et al.*, 2011). Bulk compositions taken from Bea *et al.* (2020); equivalence of labels: MG-01 = ASES21; MG-02 = ASES18; MG-03 = ASWS12. P–T fields for the mineral subassemblage Amp–Cpx–Opx–Pl (± Spl ± Fe-Ti oxides) highlighted in light colour. Mineral abbreviations after Whitney & Evans (2010). Other abbreviations: L = silicate liquid; X0/Mol = bulk composition expressed in moles (all components, except H_2O, O_2 and C, normalised to 100).

the compositional range of clinopyroxene and orthopyroxene from granoblastic aggregates and porphyroclasts were used for

the two-pyroxene thermobarometry. In addition, spot analyses of the reset compositions from these textural types and from
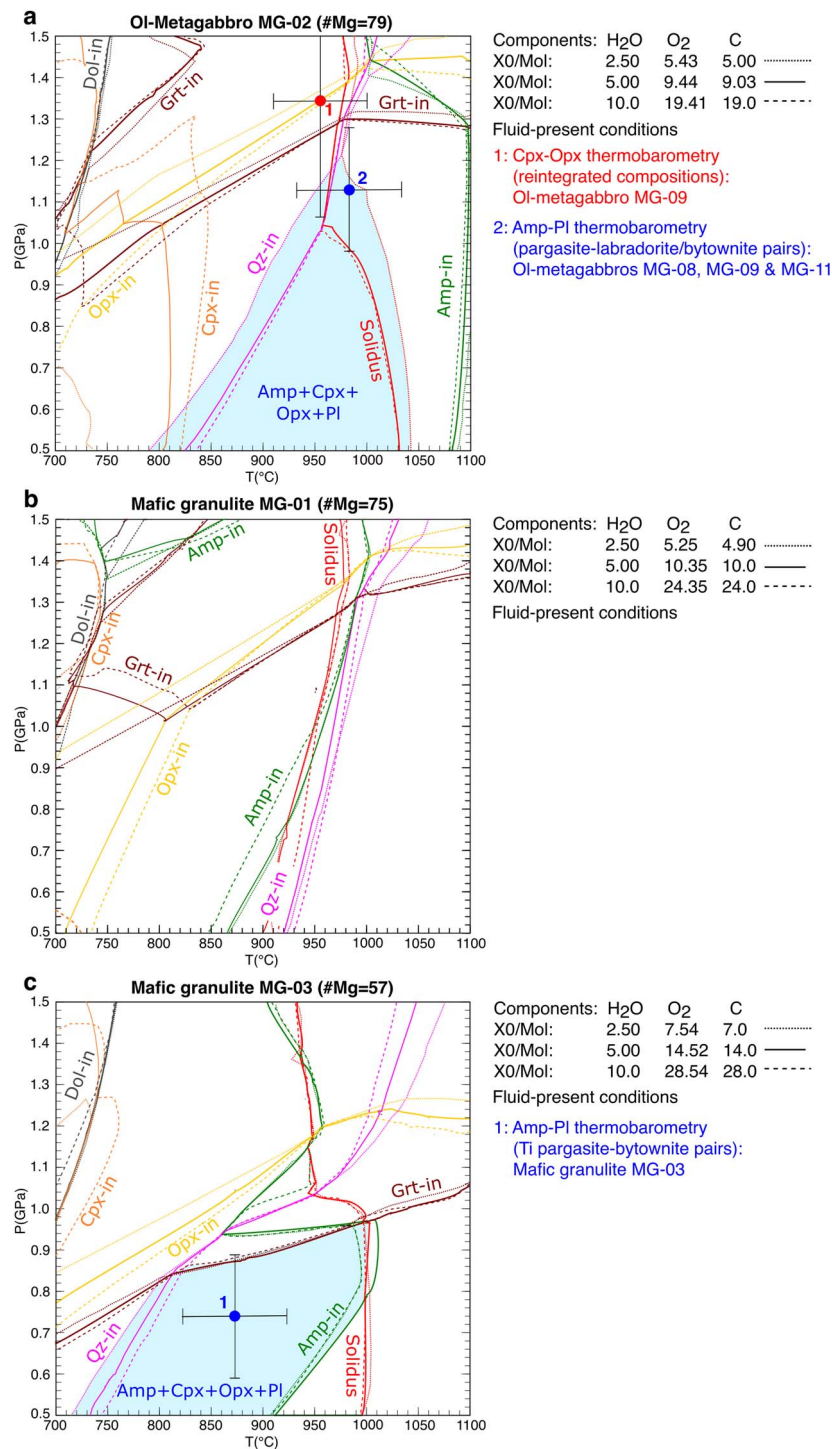
Fig. 20. Average P–T conditions and calculated P–T phase diagrams for high-grade mafic rocks from the Eastern Adrar–Suttuf Metamafic Complex. (a) Phase relations in Ol-metagabbro MG-02 with: (i) $H_2O = 2.5$ moles, $O_2 = 5.43$ moles, and $C = 5$ moles; (ii) $H_2O = 5$ moles, $O_2 = 9.44$ moles, and $C = 9.03$ moles; and (iii) $H_2O = 10$ moles, $O_2 = 19.41$ moles, and $C = 19$ moles. (b) Phase relations in mafic granulite MG-01 with: (i) $H_2O = 2.5$ moles, $O_2 = 5.25$ moles, and $C = 4.9$ moles; (ii) $H_2O = 5$ moles, $O_2 = 10.35$ moles, and $C = 10$ moles; and (iii) $H_2O = 10$ moles, $O_2 = 24.35$ moles, and $C = 24$ moles. (c) Phase relations in mafic granulite MG-03 with: (i) $H_2O = 2.5$ moles, $O_2 = 7.54$ moles, and $C = 7$ moles; (ii) $H_2O = 5$ moles, $O_2 = 14.52$ moles, and $C = 14$ moles; and (iii) $H_2O = 10$ moles, $O_2 = 28.54$ moles, and $C = 28$ moles. Refer to the caption of Fig. 19 for abbreviations and calculation methods. Bulk compositions taken from Bea *et al.* (2020). P–T fields for the mineral subassemblage Amp–Cpx–Opx–Pl (± Spl ± Fe–Ti oxides) highlighted in light colour. P–T conditions determined by amphibole–plagioclase and two-pyroxene thermobarometry (Putirka, 2008; Molina *et al.,* 2015, 2021).

clinopyroxene-orthopyroxene symplectites replacing amphibole from sample MG-03 were also used. To avoid spurious pressure estimates with two-pyroxene thermobarometry, orthopyroxene compositions with <0.01 apfu Ca were excluded from the calculations. A selection of locations of spot and areal analyses in the studied samples is presented in Appendix B (Molina *et al.,* 2024). The compositional data and the estimated P–T conditions are available in Appendixes E and F (Molina *et al.,* 2024).
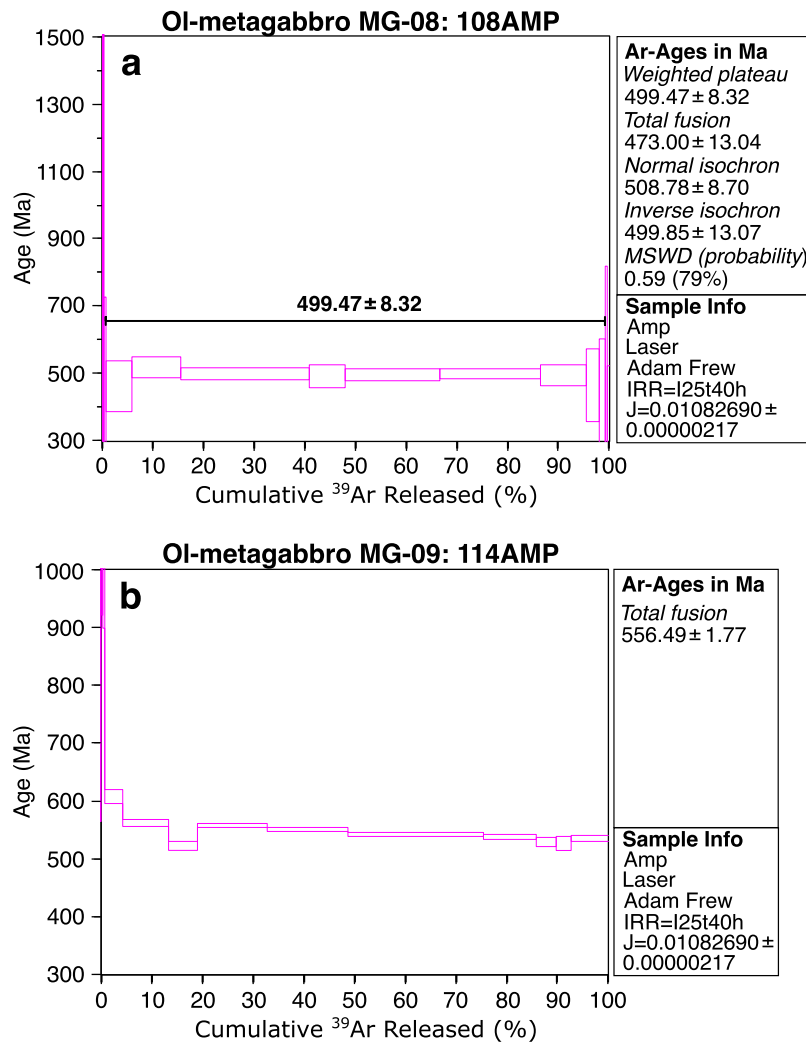
Fig. 21. ^{40}Ar–^{39}Ar age spectra of amphibole from Ol-metagabbros from the Eastern Adrar–Suttuf Metamafic Complex. (a) Mineral separate of pargasite 108AMP from sample MG-08. (b) Mineral separate of pargasite 114AMP from sample MG-09.

Clinopyroxene-orthopyroxene equilibration conditions

The P–T conditions obtained by two-pyroxene thermobarometry and the composition of the selected compositional pairs (Ca occupancies in clinopyroxene and orthopyroxene) are displayed in the diagrams from Fig. 17. The precisions by samples of the temperature estimates ($< \pm 22°C$) are better than that of the calibration indicating that compositional heterogeneities have a minor impact on the estimates. The precision for the pressure estimates is also better than the reported for the calibration in all samples ($< \pm 164$ MPa) but MG-12 (± 302 MPa, spot analyses).

Reintegrated compositional pairs of clinopyroxene and orthopyroxene grains from the granoblastic aggregates of Ol-metagabbros and mafic granulites give P–T conditions in the ranges of 1.16 ± 0.16 GPa to 1.37 ± 0.14 GPa and $959 \pm 13°C$ to $978 \pm 14°C$. These conditions are similar, within the uncertainties of the calibrations, to those obtained for reintegrated compositions of pyroxene porphyroclasts (1.32 ± 0.03 GPa and $942 \pm 16°C$). Taken all these compositional data together, an overall P–T condition of 1.28 ± 0.28 GPa and $965 \pm 45°C$ is obtained for the reintegrated compositions (hereafter, to avoid precision overestimations, the poorer precision of the two, calibration or sample, is considered for overall P–T estimates).

The P–T conditions for reset compositional pairs of pyroxenes from both granoblastic aggregates and porphyroclasts are significantly lower (overall values: 0.72 ± 0.28 GPa and $845 \pm 45°C$; ranges: 0.46 ± 0.05 GPa to 0.79 ± 0.16 GPa, and $842 \pm 22°C$ to $858 \pm 14°C$). For symplectitic aggregates of clinopyroxene and orthopyroxene after Ti pargasite from sample MG-03, a slightly lower P–T estimate of 0.28 ± 0.10 GPa and $787 \pm 9°C$ was obtained.

These thermobarometric estimations suggest that clinopyroxene and orthopyroxene from both Ol-metagabbros and mafic granulites (both granoblastic and mylonitic) were equilibrated at temperatures conditions consistent with a magmatic to UHT metamorphic transition in the deep crust and that the production of exsolution lamellae and amphibole replacements by symplectitic aggregates of pyroxenes occurred during decompression in the mid-upper crust.

Amphibole–plagioclase equilibration conditions

The average P–T conditions obtained from temperature estimates T_{A1}, T_{A2}, and T_{B2} and pressure estimates $P(T_{A1})$, $P(T_{A2})$, and $P(T_{B2})$ are displayed in the diagrams from Fig. 18. The precisions by sample for the estimated P–T conditions ($< \pm 0.07$ GPa and $< \pm 37°C$) are also significantly lower than those of the calibrations. Average P–T estimates for pargasite–labradorite/bytownite pairs (Figs. 18a-d) from granoblastic aggregates of Ol-metagabbros and mafic granulite MG-01 and porphyroclasts from mylonitic mafic granulite MG-12 range from 1.00 ± 0.02 GPa to 1.23 ± 0.04 GPa,
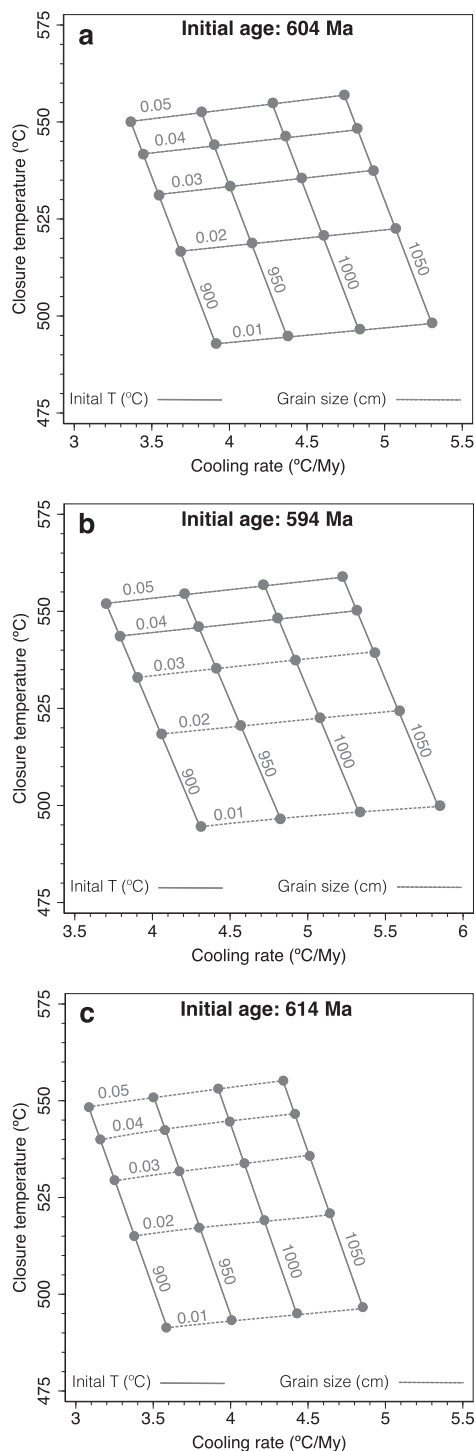
Fig. 22. ^{40}Ar–^{39}Ar closure temperatures and average cooling rates for high-grade mafic rocks from the Eastern Adrar–Suttuf Metamafic Complex. Closure temperatures and average cooling rates calculated for initial ages of 604 Ma (a), 594 Ma (b) and 614 Ma (c) using equation (9) from Dodson (1979) for a constant rate of cooling. The cooling age was set at the 499 Ma ^{40}Ar–^{39}Ar plateau age obtained from mineral separate of pargasite 108AMP from sample MG-08. Calculations were performed using amphibole parameters reported by Li et al. (2020): $E = 64.1$ kcal/mol, $D_0 = 0.024$ cm^2/s, and $A = 55$.

and from 957 ± 8°C to 1018 ± 10°C. These estimates give an overall P–T condition of 1.11 ± 0.15 GPa and 982 ± 50°C. These values are in excellent agreement with those obtained by two-pyroxene thermobarometry for reintegrated compositional pairs

of clinopyroxene and orthopyroxene grains (note a difference of ca. 170 MPa and 17°C).

Slightly lower average P–T conditions are determined for the equilibration of Ti pargasite–bytownite pairs from granoblastic aggregates of mafic granulite MG-03 and of tschermakite-bytownite pairs from porphyroclasts of mylonitic mafic granulite MG-05 (respectively, 0.74 ± 0.05 GPa and 876 ± 29°C, and 0.90 ± 0.02 GPa and 911 ± 21°C; Figs. 18a-d). In sample MG-03, there is a good agreement between temperatures determined by amphibole–plagioclase and Ti-in-amphibole thermometry that can be explained by the presence of ilmenite in its matrix (Fig. 18e; note, however, that temperatures estimated by Ti-in-amphibole thermometry for the other samples are systematically lower due to the absence of a Ti mineral phase).

To understand the mechanisms that caused the equilibration of granoblastic aggregates from sample MG-03 at lower P–T conditions, it is important to indicate that, as previously mentioned, the widespread occurrence of tiny grains of clinopyroxene and orthopyroxene precludes an unambiguous determination of the relationships between textural maturation and magmatism. However, Bea et al. (2020) have reported a gradual decrease in the pressure of magmatism towards the west of the ASMC, achieving 0.3–0.4 GPa at the contact with the Ediacaran Leucocratic Complex. In light of these relationships, the pressure differences may likely be due to a tectonic juxtaposition of lower- and mid-crustal blocks, which is consistent with the decompression-cooling path and with the context of rifting suggested for the Ediacaran magmatism (Bea et al., 2020). This is supported by the absence of garnet in sample MG-03, which implies, as discussed in the next section, that pressures could not have exceeded 1 GPa.

The average P–T conditions for the equilibration of low Ti pargasite–andesine from reactions sites in Ol-metagabbro MG-09 and mylonitic mafic granulite MG-12 (Figs. 18a-d) are 1.08 ± 0.08 GPa and 772 ± 25°C. These temperature conditions are close to those yielded by two-pyroxene thermobarometry on symplectites from sample MG-03; however, pressure estimates are significantly higher suggesting an 'apparent' isobaric cooling path. We are more confident with the decompression path model inferred from two-pyroxene thermobarometry because the Ti occupancy of amphibole is below the prescribed value for the use of the amphibole–plagioclase barometer (<0.02 apfu; Molina et al., 2015). Besides, a decompression path is more consistent with the calculated phase relationships discussed below.

Phase stability diagram calculations

The P–T stability fields determined for the mineral subassemblage Amp–Cpx–Opx–Pl (± Spl ± Fe–Ti oxides; dolomite did not appear at the relevant P–T conditions, see discussion below) present in the Ol-metagabbros and the mafic granulites from the EASMC were determined by thermodynamic modelling using the GeoPS program (Xiang & Connolly, 2022) with the internally consistent thermodynamic dataset of Holland & Powell (2011, updated version HP633) and the following mixing models: cAmph(G) for amphibole (Green et al., 2016), Cpx(HGP) for clinopyroxene, Gt(HGP) for garnet, Melt(HGP) for silicate melt, O(HGP) for olivine, Opx(HGP) for orthopyroxene and Sp(HGP) for spinel-group minerals (Holland et al., 2018), Ilm(W) for ilmenite (White et al., 2014), Fsp(C1) for plagioclase (Holland & Powell, 2003), Ep(HP11) for epidote and F for H$_2$O–CO$_2$ fluids (Holland & Powell, 2011), and dis(EF) and oCcM(EF) for carbonates (Franzolin et al., 2011).

The calculations were performed for Ol-metagabbro MG-02 (#Mg = 79; magnesium number, #Mg = 100*Mg/(Mg + Fe) atomic ratio), and mafic granulites MG-01 (#Mg = 75) and MG-03 (#Mg = 57)
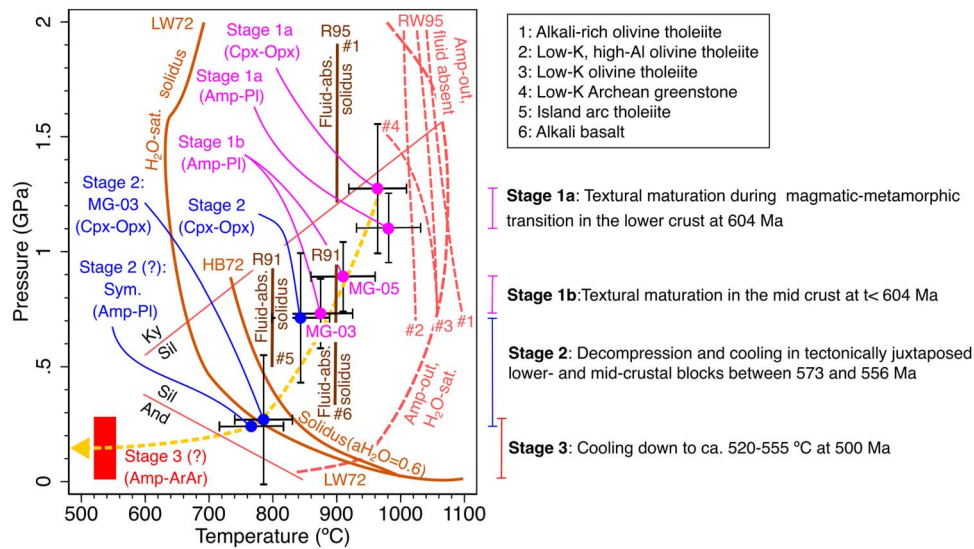
Fig. 23. P–T evolution of high-grade mafic rocks from the Eastern Adrar–Suttuf Metamafic Complex. Average P–T conditions and experimentally determined melting reactions for amphibolites. P–T conditions determined by amphibole–plagioclase and two-pyroxene thermobarometry (Putirka, 2008; Molina *et al.*, 2015, 2021). Fluid-saturated solidi for $a_{H_2O} = 1$ from Lambert & Wyllie (1972; LW72) and for $a_{H_2O} = 0.6$ from Holloway & Burnham (1972; HB72); fluid-absent solidi from Rapp (1995; R95) and Rushmer (1991; R91); amphibole-out reactions for H_2O-saturated systems from Lambert & Wyllie (1972; LW72) and fluid-absent conditions from Rapp & Watson (1995; RW95). Mineral abbreviations after Whitney & Evans (2010).

(bulk compositions taken from Bea *et al.,* 2020), assuming H_2O contents of 2.5, 5 and 10 moles (volatile components expressed as moles per 100 moles of condensed system components). For each H_2O value, *optimal contents* of C and O_2 were selected through the trial-and-error method to maximize the P–T stability fields of the mineral subassemblage Amp–Cpx–Opx–Pl; the obtained values are as follows:

Ol-metagabbro MG-02:

- $H_2O = 2.5$ moles, $O_2 = 5.43$ moles, and C = 5 moles
- $H_2O = 5$ moles, $O_2 = 9.44$ moles, and C = 9.03 moles
- $H_2O = 10$ moles, $O_2 = 19.41$ moles, and C = 19 moles

Mafic granulite MG-01:

- $H_2O = 2.5$ moles, $O_2 = 5.25$ moles, and C = 4.9 moles
- $H_2O = 5$ moles, $O_2 = 10.35$ moles, and C = 10 moles
- $H_2O = 10$ moles, $O_2 = 24.35$ moles, and C = 24 moles

Mafic granulite MG-03:

- $H_2O = 2.5$ moles, $O_2 = 7.54$ moles, and C = 7 moles
- $H_2O = 5$ moles, $O_2 = 14.52$ moles, and C = 14 moles
- $H_2O = 10$ moles, $O_2 = 28.54$ moles, and C = 28 moles

Figures 19a-c present detailed phase diagrams calculated for 5 moles of H_2O displaying the stability fields of the mineral subassemblage Amp–Cpx–Opx–Pl highlighted in light blue. The diagram from Fig. 19d illustrates how a reduction of 7 moles from the *optimal contents* of O_2 and C ($O_2 = 14.52$ moles and C = 14 moles) affects the extent of the stability field of the mineral subassemblage Amp–Cpx–Opx–Pl in *mafic granulite MG-03* with 5 moles of H_2O (compare with Fig. 19c). Simplified phase diagrams are displayed in Fig. 20 showing the loci of the solidus and the phase boundaries for the incoming of Amp, Cpx, Dol, Grt, Opx and Qz as a function of the volatile contents, as well as the phase stability fields for the mineral subassemblage Amp–Cpx–Opx–Pl, and the estimated P–T conditions for the high-grade mafic rocks from the EASMC.

Forshaw *et al.* (2019) and Hernández-Uribe *et al.* (2022), among others, have highlighted significant discrepancies between calcu-

lated and observed mineral phase compositions and abundances. However, we have verified that the GeoPS program can reasonably reproduce the P–T phase fields of mineral assemblages from experiments on hydrous mafic systems as those conducted by Ernst & Liu (1998) and Blatter *et al.* (2023) (not shown). However, it is worth mentioning that the calculated phase diagrams for the studied EASMC mafic rocks suggest an apparent instability of dolomite under granulite-facies conditions. This issue may arise from the limitations of mixing models in accommodating the compositional complexities of fluids and melts in the investigated systems, as will be discussed later. Olivine is also absent in the diagrams calculated for the Ol-metagabbro. This absence could be attributed to the cumulus nature of these rocks, as the accumulation of plagioclase, pyroxenes and amphibole might have resulted in a bulk composition undersaturated in olivine. In addition, the bulk composition of the studied rocks may have been further modified by metasomatic processes related to fluid infiltration during the growth of the symplectites upon cooling, thus complicating the computation of the phase stability relationships. Given these limitations, the analysis of the phase relationships will focus on searching for the P–T stability fields of the main mineral subassemblage Amp–Cpx–Opx–Pl that are consistent with the P–T conditions determined by classical thermobarometry.

The position of the curves for the appearance of the key mineral phases highlighted in the diagrams from Figs. 19 and 20 depends on the bulk composition of the system and the abundance of volatile components (H_2O, O_2, and C). The *solidus temperature* in Ol-metagabbro MG-02 at 1.1. GPa is ca. 960°C for 10 and 5 moles of H_2O, increasing to ca. 1000°C at 1.1. GPa for 2.5 moles of H_2O (Fig. 20a). In mafic granulites MG-01 and MG-03, the solidus positions for compositions with C/H_2O molar ratios >2 cluster around, respectively, 960°C at 1.1 GPa and 1000°C at 0.74 GPa (Figs. 20b-c). These solidus temperatures are between 60 and 100°C higher than those determined experimentally for fluid-absent conditions by Rushmer (1991) and Rapp (1995) (Fig. 23). However, a significant decrease in these temperatures occurs with decreasing the carbon abundance of the system; for example, it is displaced towards ca. 930°C at 0.74 GPa in composition MG-03 with 5 moles of H_2O and

7 moles of C (Fig. 19d), whereas for 5 moles of H_2O and 3 moles of C (not shown), the solidus temperature decreases to ca. 870°C at 0.74 GPa. In line with what has been known since the pioneering experimental works on the gabbro-granulite transition (e.g. Ringwood & Green, 1966; Green & Ringwood, 1967), the *garnet-in curves* are displaced towards higher pressures as the #Mg of the system increases; thus, the incoming of garnet occurs between 1.28 and 1.32 GPa in compositions MG-01 and MG-02 at 980°C (Figs. 20a-b), and between 0.87 and 0.90 GPa in composition MG-03 at 875°C (Figs. 19d and 20c). The *amphibole-in curves* for composition MG-02 are located at temperatures well above the solidus at pressures <1.3 GPa, with values ranging 1080–1100°C for pressures between 0.5 and 1.3 GPa (Fig. 20a). These amphibole-saturation temperatures are slightly higher than those experimentally determined at pressures >1.0 GPa by Lambert & Wyllie (1972) for H_2O-saturated systems and by Rapp & Watson (1995) for fluid-absent conditions (Fig. 23). In compositions MG-01 and MG-03, the amphibole-saturation temperatures are displaced downward by, respectively, 125°C at 1.1 GPa and 75–125°C at 0.74 GPa (Figs. 19d and 20b-c), thus being possible the appearance of low-P amphibole-absent phase fields at subsolidus conditions. The *quartz-in curves* in composition MG-01 are located at temperatures slightly above the solidus (e.g. 975–990°C at 1.1 GPa), thus leading to all subsolidus mineral assemblages being quartz-saturated (Fig. 20b). In compositions MG-02 and MG03, subsolidus quartz-free phase fields appear at pressures <1.03–1.22 GPa and < 0.88–1.03 GPa, respectively (Figs. 19d and 20a and c); thus, the quartz-in curves are located between 920 and 950°C at 1.0 GPa in composition MG-02, and between 775 and 860°C at 0.74 GPa in composition MG-03. The P–T phase fields for dolomite-bearing assemblages appear at low-temperature conditions, with *dolomite-in curves* located at <715°C and 1.0 GPa, and at <785°C and 1.5 GPa.

P–T stability fields for the mineral subassemblage Amp–Cpx–Opx–Pl are present in the Ol-metagabbro MG-02 (Fig. 20a) and the mafic granulite MG-03 (Figs. 19d and 20c), but absent in the mafic granulite MG-01 because of the stability of quartz at subsolidus conditions (Figs. 20b). They are limited by the quartz-in curve at low temperatures and the solidus at high temperatures in composition MG-02 for all the explored contents of volatile components (Fig. 20a), and in composition MG-03 for 5 moles of H_2O and 7 moles of C (Fig. 19d). For composition MG-03 with C/H_2O molar ratios >2, they are also limited by the garnet-in curve at high pressures and the amphibole-in curve at high temperatures and low pressures (Fig. 20c). Although the phase-relation calculations do not reproduce the main mineral assemblages found in the high-grade mafic rocks from the EASMC because of the apparent instability of dolomite, it is worth mentioning that the average P–T equilibration conditions for pargasite–labradorite/bytownite pairs from Ol-metagabbros, and for Ti pargasite–bytownite pairs from mafic granulite MG-03 are consistent with the absence of garnet (Figs. 20a and c); the average P–T condition for reintegrated compositions of clinopyroxene-orthopyroxene pairs from metagabbro MG-09 lies inside the stability field of garnet, but close to the garnet-in curve, thus being, within the uncertainties, consistent with the absence of garnet (Fig. 20a). Therefore, the P–T conditions determined by classical thermobarometry in the previous section are consistent with those spanned by the phase field of the mineral assemblage Amp–Cpx–Opx–Pl determined by thermodynamic equilibrium calculations. It is important to note that the absence of garnet in the magnesian metagabbros and mafic granulites can then be explained by the significant displacement towards higher pressures of the garnet incoming, while in the ferroan mafic granulites, its absence can be attributed to the

significantly lower P–T conditions of amphibole–plagioclase equilibration. These thermodynamic equilibrium calculations also support that the peak P–T conditions determined by classical thermobarometry would be close to the solidus and, therefore, that it is likely the presence of interstitial residual melts in the granoblastic aggregates of metagabbros and mafic granulites during textural maturation. Besides, it is worth noting that the cooling-decompression path inferred from two-pyroxene thermobarometry is more consistent with the calculated phase diagrams, as the positive slope of the garnet-incoming curves would imply a generalised garnet blastesis during an isobaric cooling.

However, as mentioned above, the calculated phase diagrams show that dolomite cannot be stable in the studied mafic systems at T > 720–750°C and, hence, do not support the formation of dolomite in the EASMC mafic rocks at high-temperature conditions as suggested by annealing textural evidence of dolomite grains. This problem was noted by Lamb (2005) who highlighted the instability of carbonates in the presence of quartz and orthopyroxene at granulite-facies conditions. This is in line with more recent experiments on carbonate-biotite gneisses conducted by Mityaev et al. (2022). However, the presence of dolomite and ankerite grains disseminated along grain boundaries and microfractures have been reported in many granulite-facies terrains (see review in Lamb, 2005; see also Dahlgren et al., 1993). Touret (1985) proposed that these carbonates could have been derived from carbonatitic melts (see also Touret & Huizenga, 2012, 2020), whereas Newton & Manning (2002, 2010) also suggest that a supercritical phase with no distinction between a carbonatite melt and carbonate-bearing saline fluid at high P–T conditions could be the source of the CO_2 found in fluid inclusions from granulites (see Newton, 2020, further discussion). The phase equilibria calculations performed with the thermodynamic dataset of Holland & Powell (2011) demonstrate that dolomite is not stable in the presence of H_2O–CO_2 fluids at high-temperature conditions, however, they cannot explore equilibria with immiscible carbonatite-silicate melts or with complex carbonate-saline fluids due to the lack of thermodynamic data. Therefore, the crystallisation of dolomite in the EASMC high-grade mafic rocks during the UHT event cannot be ruled out, as suggested by the presence of dolomite grains with evidence of intense textural maturation as well as the equilibration of dolomite with high-temperature minerals. Otherwise, given the decompression-cooling path inferred from two-pyroxene thermobarometry, dolomite should have crystallised at temperatures well below 700°C, i.e. after symplectite growth that is inconsistent with the textural relationships (Fig. 10b). Remarkably, as a consequence of the decompression P–T path inferred for the EASMC, the infiltration of H_2O–CO_2 fluids would have resulted in the dissolution of dolomite. This implies that fluid-absent conditions likely prevailed in the granoblastic aggregates of the main mineral assemblage Amp–Cpx–Opx–Pl–Dol (± Spl ± Fe–Ti oxides) during cooling, thus limiting the presence of fluids to the reaction sites located at the mineral grain boundaries.

^{40}Ar–^{39}Ar DATING: CONSTRAINTS ON THE TEMPERATURE–TIME EVOLUTION

$^{40}Ar/^{39}Ar$ analyses were performed on amphibole grains separated from Ol-metagabbros (mineral separates: 108AMP from sample MG-08 and 114AMP from sample MG-09) —See Appendixes G, H1 and H2 in Molina et al. (2024) for sample description and ^{40}Ar–^{39}Ar data. Samples were crushed and sieved to the

100–300 μm fraction, and the separates were washed in alcohol and deionised water. Unaltered, clean 100–150 μm grains were handpicked under a binocular microscope. The mineral concentrates were analysed by step-heating at the Western Australian Argon Isotope Facility from the Curtin University (Australia). The mean J-value (irradiation parameter) of 0.01082690 ± 0.00000217 was obtained from the Fish Canyon sanidine (age: 28.294 ± 0.037 Ma (precision at 1 s level); Renne *et al.,* 2010), used as neutron flux monitor during the irradiation procedure (see Scibiorski *et al.,* 2015, for details). Age plateaus were determined when plateaus included at least 70% of the total measured ^{39}Ar, distributed over at least three consecutive steps that agreed at a 95% confidence level and verified a probability of fit (P) of at least 0.05.

The spectrum for the mineral separate pargasite 108AMP yielded a good plateau age of 499 ± 8 Ma (precision at 2 s level) (Fig. 21a). Total fusion and normal and inverse isochrons gave an identical age within errors. The spectrum for the mineral separate pargasite 114AMP yielded progressively younger apparent ages with an increasing fraction of ^{39}Ar released (Fig. 21b), thus preventing the calculation of a plateau (total fusion age: 556 ± 2 Ma). This sample present relatively abundant alteration sites with low-Ti pargasite (Fig. 13d). This behaviour can be attributed to presence of excess ^{40}Ar in fluid inclusions entrapped in amphibole grains (c.f., Blanckenburg & Villa, 1988; Cumbest *et al.,* 1994; Wartho *et al.,* 1996), which could have been generated by the infiltration of fluids during the growth of low-Ti pargasite.

The ^{40}Ar–^{39}Ar plateau age for 108 Amp suggests that the K-Ar system in the less retrogressed pargasite grains from the EASMC metagabbro MG-08 has remained undisturbed below a certain closure temperature during the last 500 My. This closure temperature was determined by iterative calculations using the equations of Dodson (1973, 1979). For this purpose, we assumed a constant cooling rate, $\dot{r}$, expressed as follows:

$$\dot{r} = \frac{T_c - T_i}{t_c - t_i}$$

where T_c and T_i are respectively the closure and the initial temperatures, expressed in kelvin, and t_c and t_i the cooling and initial ages, expressed in Ma. This can be considered as an average cooling rate since it only involves the initial and final values. Since the exact $\dot{r}$ trajectory in the T–t space can be much more complex, this assumption supposes a substantial simplification but it can provide us a rough estimate of the temperature of closure. This was iteratively calculated using a modified version of equation (9) from Dodson (1979) for a constant rate of cooling:

$$T_c = \frac{E}{Rln\left\{AD_o\left(t_c - t_i\right)RT_c^2 / \left[Ea^2\left(t_c - t_i\right)\right]\right\}}$$

where *R, A* and *a* are respectively the gas constant, a geometric factor and the effective diffusion radius in cm, and *E* and D_o the activation energy and the pre-exponential factor of the Arrhenius type relation of the diffusion coefficient, *D*, with temperature:

$$D = D_o e^{-E/RT}$$

Calculations were performed for *a* between 0.01 and 0.05 cm and T_i between 900 and 1050°C, using amphibole parameters reported in Li *et al.* (2020): E = 64.1 kcal/mol, D_o = 0.024 cm²/s, and A = 55. The initial age was set at 604 Ma, which is the zircon crystallisation

age reported by Bea *et al.* (2020) for EASMC metagabbros from the Entajate body. This assumption is reasonable because recent melt-zircon experiments by Cambeses *et al.* (2023) and numerical modelling by Bea *et al.* (2022) predict that, in basic magmas, zircon should crystallise from melts confined in isolated pores. Therefore, it is likely that zircon saturation took place during the last stage of magma crystallisation, i.e. during the transition from magmatic to UHT metamorphic conditions when textural maturation of pargasite grains from the rock matrix of the high-grade mafic rock occurred. For this initial age, the calculated closure temperatures range from 520 to 555°C for T_i = 950–1000°C and grain size = 0.02–0.05 cm (Fig. 22a). Figures 22b and c show that this closure temperature range is very close to those obtained for initial ages of 594 and 614 Ma, suggesting that an uncertainty of ± 10 My in the initial age has a negligible impact on the estimated closure temperatures. The average cooling rates estimated for an initial age of 604 Ma range from 3.8 to 4.6°C/My (Fig. 22a; range for an average initial temperature of 975°C: 4–4.4°C/My).

Therefore, these results suggest that the deepest mafic blocks from the EASMC could have evolved from magmatic-UHT metamorphic conditions in the lower crust at 604 Ma (stage 1a; Fig. 23) to greenschist–amphibolite facies conditions in the mid-upper crust at ca. 500 Ma (stage 3; Fig. 23). Considering an average cooling rate of 4.2°C/My, the resetting of clinopyroxene-orthopyroxene compositions at 845°C could take place at ca. 573 Ma (stage 2; Fig. 23), whereas generation of low Ti pargasite–andesine at ca. 772°C in reactions sites occurred at ca. 556 Ma, which is consistent with concordant Th–U–Pb zircon ages of 570–550 Ma of metagabbros from the Entajate body, interpreted as metamorphic ages by Bea *et al.* (2020). This is noteworthy as it supports the calculated ages despite the limitations inherent in using a constant cooling rate. Therefore, according to the assumed average cooling rate, it can be inferred a duration for the UHT event in the EASMC of ca. 20 My (temperature range from 975°C, the annealing temperature, to 900°C, the lower limit of the UHT metamorphism, Harley, 1998), that is relatively short when compared to those of long-lived UHT terrains (> 30 My, Harley, 2016). In the mid-crustal block (stage 1b; Fig. 23), textural maturation should have occurred later than 604 Ma due to the younger age of the shallower magmatic intrusions from the central and western domains of the ASMC.

SUMMARY AND CONCLUSIONS

The Eastern Adrar–Suttuf Metamafic Complex contains high-grade mafic rocks that represent mafic igneous intrusions emplaced in the lower crust, with the main mineral assemblage Amp–Cpx–Opx–Pl–Dol ± Spl that was equilibrated at UHT-granulite-facies conditions (ca. 1.2 ± 0.28 GPa and 975 ± 50°C; stage 1a in Fig. 23). In addition, there are mafic blocks derived from the mid crust with the main mineral assemblage Amp–Cpx–Opx–Pl–Dol ± Fe–Ti oxides that was equilibrated at HT-granulite-facies conditions (ca. 0.82 ± 0.15 GPa and 894 ± 50°C; stage 1b in Fig. 23).

At these conditions, experimental and calculated phase relations suggest that interstitial hydrous melts could be present (Figs. 19, 20 and 23). These melts could cause the incongruent melting of olivine, which is not stable in any calculated phase fields, as well as pyroxenes. Additionally, it is likely that the melts triggered the development of An-rich spikes at the grain rims of plagioclase and assisted textural maturation of the rock matrix and local segregation of pargasite into veins. So, all these processes took place in the context of a transition from magmatic to HT-UHT-granulite-facies metamorphic conditions, as recently

proposed by Torres-Rodriguez et al. (2021) for cumulate rocks of the Nova intrusions, Albany-Fraser orogen, and Wang et al. (2022) for metatroctolite from the early Paleozoic Tongbai Orogen. In the deepest blocks, the duration of this process was relatively short (ca. 20 My, assuming a constant cooling rate of 4.2°C/My).

Although dolomite cannot be stable at granulite-facies conditions in the presence of H_2O–CO_2 fluids, the textural evidence supports an early crystallisation at high-temperature conditions that might have involved a more complex fluid or melt phase (see discussion in Touret, 1985; Newton & Manning, 2002, 2010; Touret & Huizenga, 2012, 2020; Newton, 2020). Precipitation of dolomite from externally derived CO_2 fluids is also improbable because of the low permeability of CO_2-rich fluids (e.g. Brenan & Watson, 1988; Holness & Graham, 1991; Johnson, 1991; Gibert et al., 1998) and the scarcity of carbonate veins (only one late vein was found in the mylonitic mafic granulites) despite of the widespread occurrence of dolomite. However, infiltration of saline fluids is also unlikely because of the low halogen contents of pargasite from the granoblastic aggregates. For these reasons, it is more likely that dolomite could have been formed from a locally derived CO_2-bearing phase that might be an immiscible carbonatite melt exsolved from the basic parental magma.

The EASMC experienced a decompression-cooling path (stage 2 in Fig. 23) down to the amphibolite-granulite-facies transition at ca. 556 Ma and greenschist–amphibolite-facies conditions at ca. 500 M (stage 3 in Fig. 23), being produced the tectonic juxta-position of lower- and mid-crustal blocks that is consistent with the context of rifting suggested for the Ediacaran magmatism (Bea et al., 2020). During cooling, clinopyroxene and orthopyroxene reset their composition by developing exsolution lamellae. However, Ti-rich amphiboles (pargasite, Ti pargasite and tschermakite) and calcic plagioclase (mostly labradorite and bytownite) retained their high-temperature equilibrium compositions. These mineral phases were only transformed into low-Ti pargasite and andesine at reaction sites by coupled dissolution-precipitation replacement mechanisms mediated by infiltrated reactive fluids as attested by the presence of micropores in the reaction products (Figs. 12-14) (c.f., Putnis, 2002; Putnis & Austrheim, 2013; Putnis et al., 2017; Spruzeniece et al., 2017). These fluids should have caused metaso-matism in the EASMC high-grade mafic rocks as there is clear evidence for the release of CaO and Na_2O during replacement of pla-gioclase by quartz-aluminosilicate aggregates (Figs. 12c-d) and of TiO_2, K_2O and F during replacement of Ti pargasite by aggregates of clinopyroxene, orthopyroxene, and sodic plagioclase (Figs. 14 a-b). As in this latter case, there is no clear evidence for the growth of mineral phases that could fix the released TiO_2, K_2O and fluorine it is more likely that the scale of transport should be larger than a single thin section. All these reaction textures developed in high-grade mafic rocks highlight the importance of infiltrated fluids in promoting the progress of metamorphic reactions in initially dry systems (i.e. fluid-absent conditions), as extensively discussed in the literature (e.g. Rubie, 1990; Austrheim et al., 1997; Austrheim, 1998; Scambelluri et al., 1998; Engvik et al., 2000; Molina et al., 2002; Molina & Montero, 2003; Austrheim, 2013). Accordingly, the textual relationships of the EASMC high-grade mafic rocks reveal that only those zones that were permeable to the infiltration of reactive fluids were able to develop amphibolite-facies overprints. So, the presence of Cl-bearing amphibole veins crosscutting the mylonitic banding in metagabbros indicates that the latter are prone to react when a hydrous fluid is available. By contrast, in those zones that remained closed to the infiltration of external fluids, a high-temperature history is preserved that reveals the crystallization of dolomite that survived due to the prevalence of fluid-absent conditions in the granoblastic matrix.

The lower-crustal mafic intrusions from the EASMC can represent a source of heat for granulitisation of the mid crust as they can maintain temperatures above 900°C for almost 20 My, but they could represent a sink for carbon due to the apparent stability of dolomite under fluid-absent conditions.

CONFLICT OF INTEREST STATEMENT

All authors have seen and agree with the contents of the manuscript and there is no financial interest. The authors have no conflict of interest to declare.

DATA AVAILABILITY

The data underlying this article are available in EarthChem Library, Interdisciplinary Earth Data Alliance (IEDA), at https://doi.org/10.60520/IEDA/113232.

REFERENCES

Anovitz, L. M. (1991). Al zoning in pyroxene and plagioclase: window on late prograde to early retrograde PT paths in granulite terranes. *American Mineralogist* **76**(7–8), 1328–1343.

Aranovich, L. Y., Makhluf, A. R., Manning, C. E. & Newton, R. C. (2014). Dehydration melting and the relationship between granites and granulites. *Precambrian Research* **253**, 26–37. https://doi.org/10.1016/j.precamres.2014.07.004.

Aranovich, L. Y., Makhluf, A. R., Manning, C. E., Newton, R. C. & Touret, J. L. R. (2016). Fluids, melting, granulites and granites: a controversy—reply to the commentary of J.D. Clemens, I.S. Buick and G. Stevens. *Precambrian Research* **278**, 400–404. https://doi.org/10.1016/j.precamres.2016.03.020.

Austrheim, H. (1998) Influence of fluid and deformation on metamorphism of the deep crust and consequences for the geodynamics of collision zones. In: Hacker B. R. & Liou J. G. (eds) *When continents collide: Geodynamics and geochemistry of ultrahigh-pressure rocks*. Dordrecht: Springer, pp.297–323.

Austrheim, H. (2013). Fluid and deformation induced metamorphic processes around Moho beneath continent collision zones: examples from the exposed root zone of the Caledonian mountain belt,

W Norway. *Tectonophysics* **609**, 620–635. https://doi.org/10.1016/j.tecto.2013.08.030.

Austrheim, H., Erambert, M. & Engvik, A. K. (1997). Processing of crust in the root of the Caledonian continental collision zone: the role of eclogitization. *Tectonophysics* **273**(1–2), 129–153. https://doi.org/10.1016/S0040-1951(96)00291-0.

Barnes, S. J. & Roeder, P. L. (2001). The range of spinel compositions in terrestrial mafic and ultramafic rocks. *Journal of Petrology* **42**(12), 2279–2302. https://doi.org/10.1093/petrology/42.12.2279.

Bea, F., Montero, P., Haissen, F. & El Archi, A. (2013). 2.46 Ga kalsilite and nepheline syenites from the Awsard pluton, Reguibat Rise of the West African Craton, Morocco. Generation of extremely K-rich magmas at the Archean–Proterozoic transition. *Precambrian Research* **224**, 242–254. https://doi.org/10.1016/j.precamres.2012.09.024.

Bea, F., Montero, P., Haissen, F., Rjimati, E., Molina, J. F. & Scarrow, J. H. (2014). Kalsilite-bearing plutonic rocks: the deep-seated Archean Awsard Massif of the Reguibat Rise, South Morocco, West African Craton. *Earth-Science Reviews* **138**, 1–24. https://doi.org/10.1016/j.earscirev.2014.08.003.

Bea, F., Montero, P., Haissen, F., Molina, J. F., Michard, A., Lazaro, C., Mouttaqui, A., Errami, A. & Sadki, O. (2016). First evidence for Cambrian rift-related magmatism in the West African Craton Margin: the Derraman Peralkaline Felsic Complex. *Gondwana Research* **36**, 423–438. https://doi.org/10.1016/j.gr.2015.07.017.

Bea, F., Montero, P., Haissen, F., Molina, J. F., Lodeiro, G. F., Mouttaqi, A., Kuiper, Y. D. & Chaib, M. (2020). The Archean to late Paleozoic architecture of the Oulad Dlim Massif, the main Gondwanan indenter during the collision with Laurentia. *Earth-Science Reviews* **208**, 103273. https://doi.org/10.1016/j.earscirev.2020.103273.

Bea, F., Gallastegui, G., Montero, P., Molina-Palma, J. F., Scarrow, J. H., Cuesta, A. & Gonzalez-Menendez, L. (2021). Contrasting high-Mg, high-K rocks in Central Iberia: the appinite—vaugnerite conundrum and their (non-existent) relation with arc magmatism. *Journal of Iberian Geology* **47**, 235–261. https://doi.org/10.1007/s41513-020-00152-x.

Bea, F., Bortnikov, N., Cambeses, A., Chakraborty, S., Molina, J. F., Montero, P., Morales, I., Silantiev, S. & Zinger, T. (2022). Zircon crystallization in low-Zr mafic magmas: possible or impossible? *Chemical Geology* **602**, 120898. https://doi.org/10.1016/j.chemgeo.2022.120898.

Beard, J. S. (2019). The incongruent melting and crystallization behavior of amphibole: a second peritectic reaction in Bowen's reaction series and its petrogenetic consequences. *Jeffersoniana, Virginia Museum of Natural History* **30**(1–2), 1–5.

Beard, J. S., Ragland, P. C. & Rushmer, T. (2004). Hydration crystallization reactions between anhydrous minerals and hydrous melt to yield amphibole and biotite in igneous rocks: description and implications. *The Journal of Geology* **112**(5), 617–621. https://doi.org/10.1086/422670.

Beard, J. S., Ragland, P. C. & Crawford, M. L. (2005). Using incongruent equilibrium hydration reactions to model latter-stage crystallization in plutons: examples from the Bell Island Tonalite, Alaska. *The Journal of Geology* **113**(5), 589–599. https://doi.org/10.1086/431911.

Benisek, A., Kroll, H. & Cemic, L. (2004). New developments in two-feldspar thermometry. *American Mineralogist* **89**(10), 1496–1504. https://doi.org/10.2138/am-2004-1018.

Blanckenburg, F. & Villa, I. M. (1988). Argon retentivity and argon excess in amphiboles from the garbenschists of the Western Tauern Window, Eastern Alps. *Contributions to Mineralogy and Petrology* **100**(1), 1–11. https://doi.org/10.1007/BF00399435.

Blanks, D. E., Holwell, D. A., Fiorentini, M. L., Moroni, M., Giuliani, A., Tassara, S., González-Jiménez, J. M., Boyce, A. J. & Ferrari, E. (2020). Fluxing of mantle carbon as a physical agent for metallogenic fertilization of the crust. *Nature Communications* **11**(1), 4342. https://doi.org/10.1038/s41467-020-18157-6.

Blatter, D. L., Sisson, T. W. & Hankins, W. B. (2023). Garnet stability in arc basalt, andesite, and dacite—an experimental study. *Contributions to Mineralogy and Petrology* **178**, 33. https://doi.org/10.1007/s00410-023-02008-w.

Bohlen, S. R. (1991). On the formation of granulites. *Journal of Metamorphic Geology* **9**(3), 223–229. https://doi.org/10.1111/j.1525-1314.1991.tb00518.x.

Bosch, D., Jamais, M., Boudier, F., Nicolas, A., Dautria, J.-M. & Agrinier, P. (2004). Deep and high-temperature hydrothermal circulation in the Oman Ophiolite—petrological and isotopic evidence. *Journal of Petrology* **45**(6), 1181–1208. https://doi.org/10.1093/petrology/egh010.

Bowen, N. L. (1922). The reaction principle in petrogenesis. *The Journal of Geology* **30**(3), 177–198. https://doi.org/10.1086/622871.

Brenan, J. M. & Watson, E. B. (1988). Fluids in the lithosphere, 2. Experimental constraints on CO_2 transport in dunite and quartzite at elevated PT conditions with implications for mantle and crustal decarbonation processes. *Earth and Planetary Science Letters* **91**(1–2), 141–158. https://doi.org/10.1016/0012-821X(88)90157-4.

Cambeses, A., Chakraborty, S., Jöns, N., Montero, P. & Bea, F. (2023). How does inherited zircon survive in partially molten mantle: insights on modes of magma transport in the mantle from nanoscale melt-crystal interaction experiments. *Earth and Planetary Science Letters* **601**, 117911. https://doi.org/10.1016/j.epsl.2022.117911.

Cipar, J. H., Garber, J. M., Kylander-Clark, A. R. C. & Smye, A. J. (2020). Active crustal differentiation beneath the Rio Grande Rift. *Nature Geoscience* **13**(11), 758–763. https://doi.org/10.1038/s41561-020-0640-z.

Clark, C., Fitzsimons, I. C. W., Healy, D. & Harley, S. L. (2011). How does the continental crust get really hot? *Elements* **7**(4), 235–240. https://doi.org/10.2113/gselements.7.4.235.

Clemens, J. D., Buick, I. S. & Stevens, G. (2016). Fluids, melting, granulites and granites: a commentary. *Precambrian Research* **278**, 394–399. https://doi.org/10.1016/j.precamres.2016.01.001.

Cumbest, R. J., Johnson, E. L. & Onstott, T. C. (1994). Argon composition of metamorphic fluids: implications for $^{40}Ar/^{39}Ar$ geochronology. *Geological Society of America Bulletin* **106**, 942–951. https://doi.org/10.1130/0016-7606(1994)106<0942:ACOMFI>2.3.CO;2.

Czamanske, G. K. & Wones, D. R. (1973). Oxidation during magmatic differentiation, Finnmarka complex, Oslo area, Norway: part 2, the mafic silicates1. *Journal of Petrology* **14**(3), 349–380. https://doi.org/10.1093/petrology/14.3.349.

Dahlgren, S., Bogoch, R., Magaritz, M. & Michard, A. (1993). Hydrothermal dolomite marbles associated with charnockitic magmatism in the Proterozoic Bamble Shear Belt, South Norway. *Contributions to Mineralogy and Petrology* **113**, 394–409. https://doi.org/10.1007/BF00286930.

Dale, J., Powell, R., White, R. W., Elmer, F. L. & Holland, T. J. B. (2005). A thermodynamic model for Ca–Na clinoamphiboles in $Na_2O–CaO–FeO–MgO–Al_2O_3–SiO_2–H_2O–O$ for petrological calculations. *Journal of Metamorphic Geology* **23**(8), 771–791. https://doi.org/10.1111/j.1525-1314.2005.00609.x.

De Haas, G.-J. L., Nijland, T. G., Valbracht, P. J., Maijer, C., Verschure, R. & Andersen, T. (2002). Magmatic versus metamorphic origin of olivine-plagioclase coronas. *Contributions to Mineralogy and Petrology* **143**(5), 537–550. https://doi.org/10.1007/s00410-002-0362-9.

Dharmapriya, P. L., Kriegsman, L. M. & Malaviarachchi, S. P. K. (2021). Spatial distribution of ultrahigh-temperature granulites of the Highland Complex of Sri Lanka: lowermost continental crust above an ultrahot palaeo-Moho. *Lithos* **404-405**, 106484. https://doi.org/10.1016/j.lithos.2021.106484.

Dodson, M. H. (1973). Closure temperature in cooling geochronological and petrological systems. *Contributions to Mineralogy and Petrology* **40**, 259–274. https://doi.org/10.1007/BF00373790.

Dodson, M. H. (1979). Theory of cooling ages. In: Jäger, E. & Hunziker, J. C. (eds) *Lectures in Isotope Geology*. Berlin, Heidelberg: Springer, pp. 194–202. https://doi.org/10.1007/978-3-642-67161-6_14.

Drüppel, K., Von Seckendorff, V. & Okrusch, M. (2001). Subsolidus reaction textures in the anorthositic rocks of the southern part of the Kunene Intrusive Complex, NW Namibia. *European Journal of Mineralogy* **13**(2), 289–309. https://doi.org/10.1127/935-1221/01/0013-0289.

Engvik, A. K., Austrheim, H. & Andersen, T. B. (2000). Structural, mineralogical and petrophysical effects on deep crustal rocks of fluid-limited polymetamorphism, Western Gneiss Region, Norway. *Journal of the Geological Society* **157**(1), 121–134. https://doi.org/10.1144/jgs.157.1.121.

Ernst, W. G. & Liu, J. (1998). Experimental phase-equilibrium study of Al- and Ti-contents of calcic amphibole in MORB—a semiquantitative thermobarometer. *American Mineralogist* **83**(9–10), 952–969. https://doi.org/10.2138/am-1998-9-1004.

Forshaw, J. B., Waters, D. J., Pattison, D. R. M., Palin, R. M. & Gopon, P. (2019). A comparison of observed and thermodynamically predicted phase equilibria and mineral compositions in mafic granulites. *Journal of Metamorphic Geology* **37**(2), 153–179. https://doi.org/10.1111/jmg.12454.

Franzolin, E., Schmidt, M. W. & Poli, S. (2011). Ternary Ca–Fe–Mg carbonates: subsolidus phase relations at 3.5 GPa and a thermodynamic solid solution model including order/disorder. *Contributions to Mineralogy and Petrology* **161**, 213–227. https://doi.org/10.1007/s00410-010-0527-x.

Frost, B. R. & Chacko, T. (1989). The granulite uncertainty principle: limitations on thermobarometry in granulites. *The Journal of Geology* **97**(4), 435–450. https://doi.org/10.1086/629321.

Frost, B. R. & Frost, C. D. (2008). On charnockites. *Gondwana Research* **13**(1), 30–44. https://doi.org/10.1016/j.gr.2007.07.006.

Frost, B. R., Frost, C. D. & Touret, J. L. R. (1989) Magmas as a source of heat and fluids in granulite metamorphism. In: Bridgwater D. (ed) *Fluid Movements—Element transport and the composition of the Deep Crust*. Dordrecht: Springer,, pp.1–18.

Gallien, F., Mogessie, A., Hauzenberger, C. A., Bjerg, E., Delpino, S. & Castro de Machuca, B. (2012). On the origin of multi-layer coronas between olivine and plagioclase at the gabbro–granulite transition, Valle Fértil–La Huerta Ranges, San Juan Province, Argentina. *Journal of Metamorphic Geology* **30**(3), 281–302. https://doi.org/10.1111/j.1525-1314.2011.00967.x.

Gärtner, A., Villeneuve, M., Linnemann, U., El Archi, A. & Bellon, H. (2013). An exotic terrane of Laurussian affinity in the Mauritanides and Souttoufides (Moroccan Sahara). *Gondwana Research* **24**, 687–699. https://doi.org/10.1016/j.gr.2012.12.019.

Gärtner, A., Villeneuve, M., Linnemann, U., Gerdes, A., Youbi, N., Guillou, O. & Rjimati, E.-C. (2016). History of the West African Neoproterozoic Ocean: key to the geotectonic history of circum-Atlantic Peri-Gondwana (Adrar Souttouf Massif, Moroccan Sahara). *Gondwana Research* **29**, 220–233. https://doi.org/10.1016/j.gr.2014.11.011.

Gibert, F., Guillaume, D. & Laporte, D. (1998). Importance of fluid immiscibility in the H_2O–NaCl–CO_2 system and selective CO_2 entrapment in granulites: experimental phase diagram at 5–7 kbar, 900°C and wetting textures. *European Journal of Mineralogy* **10**(6), 1109–1124. https://doi.org/10.1127/ejm/10/6/1109.

Gibson, G. M. & Ireland, T. R. (1995). Granulite formation during continental extension in Fiordland, New Zealand. *Nature* **375**(6531), 479–482. https://doi.org/10.1038/375479a0.

Green, D. H. & Ringwood, A. E. (1967). An experimental investigation of the gabbro to eclogite transformation and its petrological applications. *Geochimica et Cosmochimica Acta* **31**(5), 767–833. https://doi.org/10.1016/S0016-7037(67)80031-0.

Green, E. C. R., White, R. W., Diener, J. F. A., Powell, R., Holland, T. J. B. & Palin, R. M. (2016). Activity–composition relations for the calculation of partial melting equilibria in metabasic rocks. *Journal of Metamorphic Geology* **34**(9), 845–869. https://doi.org/10.1111/jmg.12211.

Haissen, F., Cambeses, A., Montero, P., Bea, F., Dilek, Y. & Mouttaqi, A. (2016). The Archean kalsilite-nepheline syenites of the Awsard Intrusive Massif (Reguibat Shield, West African Craton, Morocco) and its relationship to the alkaline magmatism of Africa. *Journal of African Earth Sciences* **127**, 16–50. https://doi.org/10.1016/j.jafrearsci.2016.08.019.

Haissen, F., Montero, P., Cambeses, A., Bea, F., Molina, J. F., Mouttaqi, A., Gonzalez-Lodeiro, F., Sadki, O. & Errami, A. (2018). Petrogenesis of Derraman peralkaline granite (Oulad Dlim Massif, West African Craton Margin, Morocco): new constraints from zircon Hf and O isotopic compositions. *Comptes Rendus Geoscience* **350**(6), 236–244. https://doi.org/10.1016/j.crte.2018.06.007.

Harley, S. L. (1998). Ultrahigh temperature granulite metamorphism (1050°C, 12 kbar) and decompression in garnet (Mg70)-orthopyroxene-sillimanite gneisses from the Rauer Group, East Antarctica. *Journal of Metamorphic Geology* **16**(4), 541–562. https://doi.org/10.1111/j.1525-1314.1998.00155.x.

Harley, S. L. (2004). Extending our understanding of ultrahigh temperature crustal metamorphism. *Journal of Mineralogical and Petrological Sciences* **99**(4), 140–158. https://doi.org/10.2465/jmps.99.140.

Harley, S. L. (2008). Refining the P–T records of UHT crustal metamorphism. *Journal of Metamorphic Geology* **26**(2), 125–154. https://doi.org/10.1111/j.1525-1314.2008.00765.x.

Harley, S. L. (2016). A matter of time: the importance of the duration of UHT metamorphism. *Journal of Mineralogical and Petrological Sciences* **111**(2), 50–72. https://doi.org/10.2465/jmps.160128.

Harlov, D. E. & Austrheim, H. (2013) Metasomatism and the chemical transformation of rock: rock–mineral–fluid interaction in terrestrial and extraterrestrial environments. In: Harlov D. E. & Austrheim H. (eds) *Metasomatism and the Chemical Transformation of Rock*. Berlin, Heidelberg: Springer, pp.1–16.

Hernández-Uribe, D., Spera, F. J., Bohrson, W. A. & Heinonen, J. S. (2022). A comparative study of two-phase equilibria modeling tools: MORB equilibrium states at variable pressure and H_2O concentrations. *American Mineralogist* **107**(9), 1789–1806. https://doi.org/10.2138/am-2022-8211.

Holland, T. & Blundy, J. (1994). Non-ideal interactions in calcic amphiboles and their bearing on amphibole–plagioclase thermometry. *Contributions to Mineralogy and Petrology* **116**, 433–447. https://doi.org/10.1007/BF00310910.

Holland, T. & Powell, R. (2003). Activity–composition relations for phases in petrological calculations: an asymmetric multicomponent formulation. *Contributions to Mineralogy and Petrology* **145**, 492–501. https://doi.org/10.1007/s00410-003-0464-z.

Holland, T. J. B. & Powell, R. (2011). An improved and extended internally consistent thermodynamic dataset for phases of petrological interest, involving a new equation of state for solids.

Journal of Metamorphic Geology **29**(3), 333–383. https://doi.org/10.1111/j.1525-1314.2010.00923.x.

Holland, T. J. B., Green, E. C. R. & Powell, R. (2018). Melting of peridotites through to granites: a simple thermodynamic model in the system KNCFMASHTOCr. *Journal of Petrology* **59**(5), 881–900. https://doi.org/10.1093/petrology/egy048.

Holloway, J. R. & Burnham, C. W. (1972). Melting relations of basalt with equilibrium water pressure less than total pressure. *Journal of Petrology* **13**(1), 1–29. https://doi.org/10.1093/petrology/13.1.1.

Holness, M. B. & Graham, C. M. (1991). Equilibrium dihedral angles in the system H_2O–CO_2–NaCl–calcite, and implications for fluid flow in metamorphism. *Contributions to Mineralogy and Petrology* **108**, 368–383. https://doi.org/10.1007/BF00285944.

Holness, M. B., Cheadle, M. J. & Mckenzie, D. A. N. (2005). On the use of changes in dihedral angle to decode late-stage textural evolution in cumulates. *Journal of Petrology* **46**(8), 1565–1583. https://doi.org/10.1093/petrology/egi026.

Holness, M. B., Nielsen, T. F. D. & Tegner, C. (2007). Textural maturity of cumulates: a record of chamber filling, liquidus assemblage, cooling rate and large-scale convection in mafic layered intrusions. *Journal of Petrology* **48**(1), 141–157.

Huppert, H. E. & Sparks, S. J. (1989). The generation of granitic magmas by intrusion of basalt into continental crust. *Journal of Petrology* **29**, 599–624. https://doi.org/10.1093/petrology/29.3.599.

Joesten, R. (1986). The role of magmatic reaction, diffusion and annealing in the evolution of coronitic microstructure in troctolitic gabbro from Risör, Norway. *Mineralogical Magazine* **50**(357), 441–467. https://doi.org/10.1180/minmag.1986.050.357.08.

Johnson, E. L. (1991). Experimentally determined limits for H_2O–CO_2–NaCl immiscibility in granulites. *Geology* **19**, 925–928. https://doi.org/10.1130/0091-7613(1991)019<0925:EDLFHO>2.3.CO;2.

Keevil, H. A., Namur, O. & Holness, M. B. (2020). Microstructures and late-stage magmatic processes in layered mafic intrusions: Symplectites from the sept Iles intrusion, Quebec, Canada. *Journal of Petrology* **61**(7), egaa071. https://doi.org/10.1093/petrology/egaa071.

Kelsey, D. E. (2008). On ultrahigh-temperature crustal metamorphism. *Gondwana Research* **13**(1), 1–29. https://doi.org/10.1016/j.gr.2007.06.001.

Kelsey, D. E. & Hand, M. (2015). On ultrahigh temperature crustal metamorphism: phase equilibria, trace element thermometry, bulk composition, heat sources, timescales and tectonic settings. *Geoscience Frontiers* **6**(3), 311–356. https://doi.org/10.1016/j.gsf.2014.09.006.

Koepke, J., Feig, S. & Snow, J. (2005a). Late stage magmatic evolution of oceanic gabbros as a result of hydrous partial melting: evidence from the ocean drilling program (ODP) leg 153 drilling at the Mid-Atlantic Ridge. *Geochemistry, Geophysics, Geosystems* **6**(2), Q02001. https://doi.org/10.1029/2004GC000805.

Koepke, J., Feig, S. T. & Snow, J. (2005b). Hydrous partial melting within the lower oceanic crust. *Terra Nova* **17**(3), 286–291. https://doi.org/10.1111/j.1365-3121.2005.00613.x.

Koepke, J., Berndt, J., Horn, I., Fahle, J. & Wolff, P. E. (2014). Partial melting of oceanic gabbro triggered by migrating water-rich fluids: a prime example from the Oman ophiolite. *Geological Society, London, Special Publications* **392**(1), 195–212. https://doi.org/10.1144/SP392.10.

Lamb, W. (2005) Carbonates in feldspathic gneisses from the granulite facies: implications for the formation of CO_2-rich fluid inclusions. In: Thomas H. (ed) *Metamorphism and Crustal Evolution: Papers in Honour of Prof. RS Sharma*. New Delhi: Atlantic, pp.163–181.

Lambert, I. B. & Wyllie, P. J. (1972). Melting of gabbro (quartz eclogite) with excess water to 35 kilobars, with geological applications. *The Journal of Geology* **80**(6), 693–708. https://doi.org/10.1086/627795.

Le Maitre, R. W. (1989) *A Classification of Igneous Rocks and Glossary of Terms: Recommendations of the International Union of Geological Sciences Subcommission on the Systematics of Igneous Rocks*. Oxford: Blackwell.

Lécorché, J. P., Bronner, G., Dallmeyer, R. D., Rocci, G. & Roussel, J. (1991) The Mauritanide Orogen and its Northern Extensions (Western Sahara and Zemmour), West Africa. In: Dallmeyer R. D. & Lécorché J. P. (eds) *The West African Orogens and Circum-Atlantic Correlatives*. Springer, Berlin, Heidelberg, pp.187–227.

Lei, H. & Xu, H. (2018). A review of ultrahigh temperature metamorphism. *Journal of Earth Science* **29**(5), 1167–1180. https://doi.org/10.1007/s12583-018-0846-9.

Li, J., Pourteau, A., Li, Z., Jourdan, F., Nordsvan, A. R., Collins, W. J. & Volante, S. (2020). Heterogeneous exhumation of the Mount Isa orogen in NE Australia after 1.6 Ga Nuna assembly: new high-precision $^{40}Ar/^{39}Ar$ thermochronological constraints. *Tectonics* **39**(12), e2020TC006129. https://doi.org/10.1029/2020TC006129.

Liao, Y., Wei, C. & Rehman, H. U. (2021). Titanium in calcium amphibole: behavior and thermometry. *American Mineralogist* **106**(2), 180–191. https://doi.org/10.2138/am-2020-7409.

Lindsley, D. H. (1983). Pyroxene thermometry. *American Mineralogist* **68**(5–6), 477–493.

Maier, W. D., Barnes, S.-J., Muir, D., Savard, D., Lahaye, Y. & Smith, W. D. (2021). Formation of Bushveld anorthosite by reactive porous flow. *Contributions to Mineralogy and Petrology* **176**(1), 1–12. https://doi.org/10.1007/s00410-020-01760-7.

Mercier, J. C. C., Benoit, V. & Girardeau, J. (1984). Equilibrium state of diopside-bearing harzburgites from ophiolites: geobarometric and geodynamic implications. *Contributions to Mineralogy and Petrology* **85**, 391–403. https://doi.org/10.1007/BF01150295.

Michard, A., Hoepffner, C., Soulaimani, A. & Baidder, L. (2008) *The Variscan belt*. In: Michard A., Saddiqi O., Chalouan A. & Lamotte D. F. (eds) *Continental evolution: The geology of Morocco*. Berlin, Heidelberg: Springer, pp.65–132.

Michard, A., Soulaimani, A., Hoeffner, C., Ouanaimi, H., Rjimati, E. C., Saddiqi, O. *et al.* (2010). The south-western branch of the Variscan belt: evidence from Morocco. *Tectonophysics* **492**, 1–24. https://doi.org/10.1016/j.tecto.2010.05.021.

Mityaev, A. S., Safonov, O. G., Varlamov, D. A. & Van Reenen, D. D. (2022). Partial melting of carbonate–biotite gneiss at the conditions of the continental crust: experimental and thermodynamic modeling. *Petrology* **30**(3), 278–304. https://doi.org/10.1134/S0869591122030067.

Molina, J. F. & Montero, P. (2003). The behavior of trace-elements in high-P mineral assemblages: a LA-ICP-MS study of mafic rocks from the Nevado-Filábride complex. *Schweizerische Mineralogische und Petrographische Mitteilungen* **83**, 97–109.

Molina, J. F., Austrheim, A., Glodny, J. & Rusin, A. (2002). The eclogites of the Marun-Keu Complex, Polar Urals (Russia): fluid control on reaction kinetics and metasomatism during high-p metamorphism. *Lithos* **61**, 55–78. https://doi.org/10.1016/S0024-4937(02)00070-1.

Molina, J. F., Scarrow, J. H., Montero, P. G. & Bea, F. (2009). High-Ti amphibole as a petrogenetic indicator of magma chemistry: evidence for mildly alkalic-hybrid melts during evolution of Variscan basic–ultrabasic magmatism of Central Iberia. *Contributions to Mineralogy and Petrology* **158**(1), 69–98. https://doi.org/10.1007/s00410-008-0371-4.

Molina, J. F., Moreno, J. A., Castro, A., Rodriguez, C. A. & Fershtater, G. B. (2015). Calcic amphibole thermobarometry in metamorphic and igneous rocks: new calibrations based on plagioclase/amphibole Al-Si partitioning and amphibole/liquid mg partitioning. *Lithos* **232**, 286–305. https://doi.org/10.1016/j.lithos.2015.06.027.

Molina, J. F., Bea, F., Montero, P., Haissen, F., González-Lodeiro, F., Errami, A., Sadki, O., Moreno, J. A., Cambeses, A. & Mouttaqi, A. (2018). High-P amphibolite-facies metamorphism in the Adrar–Souttouf metamafic complex, Oulad Dlim Massif (West African Craton Margin, Morocco). *Comptes Rendus Geoscience* **350**(6), 245–254. https://doi.org/10.1016/j.crte.2018.05.005.

Molina, J. F., Cambeses, A., Moreno, J. A., Morales, I., Montero, P. & Bea, F. (2021). A reassessment of the amphibole–plagioclase NaSi-CaAl exchange thermometer with applications to igneous and high-grade metamorphic rocks. *American Mineralogist* **106**(5), 782–800. https://doi.org/10.2138/am-2021-7400.

Molina, J. F., Bea, F., Montero, P., Haissen, F., Barcos, L., Cambeses, A., Morales, I., Repczynska, M. M., Sadki, O. & García-Casco, A. (2024). Mineralogical, thermobarometric and A-Ar data of metagabbros and mafic granulites from the Ediacaran Adrar–Suttuf Metamafic Complex, NW Margin of the West African Craton (Southern Morocco). Version 1.0. *Interdisciplinary Earth Data Alliance (IEDA)* . https://doi.org/10.60520/IEDA/113232 Accessed 2024-05-05.

Montero, P., Haissen, F., El Archi, A., Rjimati, E. & Bea, F. (2014). Timing of Archean crust formation and cratonization in the Awsard-Tichla zone of the NW Reguibat Rise, West African Craton. A SHRIMP, Nd-Sr isotopes, and geochemical reconnaissance study. *Precambrian Research* **242**, 112–137. https://doi.org/10.1016/j.precamres.2013.12.013.

Montero, P., Haissen, F., Mouttaqui, A., Molina, J. F., Errami, A., Sadki, O., Cambeses, A. & Bea, F. (2016). Contrasting SHRIMP U-Pb zircon ages of two carbonatite complexes from the peri-cratonic terranes of the Reguibat Shield: implications for the lateral extension of the West African Craton. *Gondwana Research* **38**, 238–250. https://doi.org/10.1016/j.gr.2015.12.005.

Montero, P., Bea, F., Haissen, F., Molina-Palma, J. F., Gonzalez Lodeiro, F., Mouttaqi, A. & Errami, A. (2018). Dorsale Reguibat et Massif des Oulad Dlim, l'avancée des connaisances. *Geologues* **194**, 1–5.

Müller, S., Garbe-Schönberg, D., Koepke, J. & Hoernle, K. (2022). A reference section through fast-spread lower oceanic crust, Wadi Gideah, Samail ophiolite (Sultanate of Oman): trace element systematics and REE crystallization temperatures—implications for hybrid crustal accretion. *Journal of Geophysical Research: Solid Earth* **127**(3), e2021JB022699. https://doi.org/10.1029/2021JB022699.

Munnikhuis, J. K., Daczko, N. R. & Langone, A. (2023). Open system reaction between hydrous melt and gabbroic rock in the Finero Mfic Complex. *Lithos* **440-441**, 107027. https://doi.org/10.1016/j.lithos.2023.107027.

Müntener, O., Hermann, J. & Trommsdorff, V. (2000). Cooling history and exhumation of lower-crustal granulite and upper mantle (Malenco, Eastern Central Alps). *Journal of Petrology* **41**(2), 175–200. https://doi.org/10.1093/petrology/41.2.175.

Newton, R. C. (2020). Young and old granulites: a volatile connection. *The Journal of Geology* **128**, 395–413. https://doi.org/10.1086/711026.

Newton, R. C. & Manning, C. E. (2002). Experimental determination of calcite solubility in H_2O–NaCl solutions at deep crust/upper mantle pressures and temperatures: implications for metasomatic processes in shear zones. *American Mineralogist* **87**, 1401–1409. https://doi.org/10.2138/am-2002-1016.

Newton, R. C. & Manning, C. E. (2010). Role of saline fluids in deep-crustal and upper-mantle metasomatism: insights from experimental studies. *Geofluids* **10**(1–2), 58–72. https://doi.org/10.1111/j.1468-8123.2009.00275.x.

Newton, R. C., Touret, J. L. R. & Aranovich, L. Y. (2014). Fluids and H_2O activity at the onset of granulite facies metamorphism. *Precambrian Research* **253**, 17–25. https://doi.org/10.1016/j.precamres.2014.06.009.

Otten, M. T. (1984). The origin of brown hornblende in the Artfjället gabbro and dolerites. *Contributions to Mineralogy and Petrology* **86**(2), 189–199. https://doi.org/10.1007/BF00381846.

Pattison, D. R. M., Chacko, T., Farquhar, J. & McFarlane, C. R. M. (2003). Temperatures of granulite-facies metamorphism: constraints from experimental phase equilibria and thermobarometry corrected for retrograde exchange. *Journal of Petrology* **44**, 867–900. https://doi.org/10.1093/petrology/44.5.867.

Petterson, M. G. (2010). A review of the geology and tectonics of the Kohistan Island Arc, North Pakistan. *Geological Society, London, Special Publications* **338**(1), 287–327. https://doi.org/10.1144/SP338.14.

Pownall, J. M. (2015). UHT metamorphism on Seram, Eastern Indonesia: reaction microstructures and P–T evolution of spinel-bearing garnet–sillimanite granulites from the Kobipoto Complex. *Journal of Metamorphic Geology* **33**(9), 909–935. https://doi.org/10.1111/jmg.12153.

Putirka, K. (2008). Thermometers and barometers for volcanic systems. *Reviews in Mineralogy and Geochemistry* **69**, 61–120. https://doi.org/10.2138/rmg.2008.69.3.

Putnis, A. (2002). Mineral replacement reactions: from macroscopic observations to microscopic mechanisms. *Mineralogical Magazine* **66**(5), 689–708. https://doi.org/10.1180/0026461026650056.

Putnis, A. (2009). Mineral replacement reactions. *Reviews in Mineralogy and Geochemistry* **70**, 87–124. https://doi.org/10.2138/rmg.2009.70.3.

Putnis, A. & Austrheim, H. (2013) Mechanisms of metasomatism and metamorphism on the local mineral scale: the role of dissolution-reprecipitation during mineral re-equilibration. In: Harlov D. E. & Austrheim H. (eds) *Metasomatism and the chemical transformation of rock*. Berlin, Heidelberg: Springer, pp.141–170.

Putnis, A., Jamtveit, B. & Austrheim, H. (2017). Metamorphic processes and seismicity: the Bergen Arcs as a natural laboratory. *Journal of Petrology* **58**(10), 1871–1898. https://doi.org/10.1093/petrology/egx076.

Rapp, R. P. (1995). Amphibole-out phase boundary in partially melted metabasalt, its control over liquid fraction and composition, and source permeability. *Journal of Geophysical Research: Solid Earth* **100**(B8), 15601–15610. https://doi.org/10.1029/95JB00913.

Rapp, R. P. & Watson, E. B. (1995). Dehydration melting of metabasalt at 8-32 kbar: implications for continental growth and crust-mantle recycling. *Journal of Petrology* **36**(4), 891–931. https://doi.org/10.1093/petrology/36.4.891.

Ray, S., Tiwari, A. K. & Sarkar, T. (2021). Ultrahigh-temperature mafic granulites from the Madurai block, Southern India: constraints from conventional thermobarometry, pseudosection analysis, and rare earth element-based thermometry. *Geological Journal* **56**(7), 3720–3744. https://doi.org/10.1002/gj.4124.

Renne, P. R., Mundil, R., Balco, G., Min, K. & Ludwig, K. R. (2010). Joint determination of ^{40}K decay constants and $^{40}Ar^*/^{40}K$ for the Fish Canyon sanidine standard, and improved accuracy for $^{40}Ar/^{39}Ar$ geochronology. *Geochimica et Cosmochimica Acta* **74**(18), 5349–5367. https://doi.org/10.1016/j.gca.2010.06.017.

Ringwood, A. E. & Green, D. H. (1966). An experimental investigation of the gabbro-eclogite transformation and some

geophysical implications. *Tectonophysics* **3**(5), 383–427. https://doi.org/10.1016/0040-1951(66)90009-6.

Robinson, P., Spear, F. S., Schumacher, J. C., Laird, J., Klein, C., Evans, B. W. & Doolan, B. L. (1982). Phase relations of metamorphic amphiboles: natural occurrence and theory. *Reviews in Mineralogy* **9B**, 1–228. https://doi.org/10.1515/9781501508196-005.

Rubie, D. C. (1990) Role of kinetics in the formation and preservation of eclogites. In: Carswell D. A. (ed) *Eclogite Facies Rocks*. Glasgow: Blackie, pp. 111–140.

Rushmer, T. (1991). Partial melting of two amphibolites: contrasting experimental results under fluid-absent conditions. *Contributions to Mineralogy and Petrology* **107**, 41–59. https://doi.org/10.1007/BF00311184.

Sajeev, K., Osanai, Y., Kon, Y. & Itaya, T. (2009). Stability of pargasite during ultrahigh-temperature metamorphism: a consequence of titanium and REE partitioning. *American Mineralogist* **94**(4), 535–545. https://doi.org/10.2138/am.2009.2815.

Sandiford, M. & Powell, R. (1986). Deep crustal metamorphism during continental extension: modern and ancient examples. *Earth and Planetary Science Letters* **79**(1–2), 151–158. https://doi.org/10.1016/0012-821X(86)90048-8.

Scambelluri, M., Pennacchioni, G. & Philippot, P. (1998). Salt-rich aqueous fluids formed during eclogitization of metabasites in the Alpine continental crust (Austroalpine Mt. Emilius unit, Italian Western Alps). *Lithos* **43**(3), 151–167. https://doi.org/10.1016/S0024-4937(98)00011-5.

Schmitz, M. D. & Bowring, S. A. (2003). Ultrahigh-temperature metamorphism in the lower crust during Neoarchean Ventersdorp rifting and magmatism, Kaapvaal craton, Southern Africa. *Geological Society of America Bulletin* **115**(5), 533–548. https://doi.org/10.1130/0016-7606(2003)115<0533:UMITLC>2.0.CO;2.

Scibiorski, E., Tohver, E. & Jourdan, F. (2015). Rapid cooling and exhumation in the western part of the Mesoproterozoic Albany-Fraser Orogen, Western Australia. *Precambrian Research* **265**, 232–248. https://doi.org/10.1016/j.precamres.2015.02.005.

Sougy, J. (1962a). Contribution à l'étude géologique des Guelb Bou Leriah (region d'Aoucert, Sahara Espagnol). *Bulletin de la Société Géologique de France* **S7-IV**(3), 436–445. https://doi.org/10.2113/gssgfbull.S7-IV.3.436.

Sougy, J. (1962b). West African fold belt. *Geological Society of America Bulletin* **73**(7), 871–876. https://doi.org/10.1130/0016-7606(1962)73[871:WAFB]2.0.CO;2.

Spear, F. S. & Kimball, K. L. (1984). RECAMP—a Fortran IV program for estimating Fe^{3+} contents in amphiboles. *Computers & Geosciences* **10**(2–3), 317–325. https://doi.org/10.1016/0098-3004(84)90029-3.

Spruzeniece, L., Piazolo, S., Daczko, N. R., Kilburn, M. R. & Putnis, A. (2017). Symplectite formation in the presence of a reactive fluid: insights from hydrothermal experiments. *Journal of Metamorphic Geology* **35**(3), 281–299. https://doi.org/10.1111/jmg.12231.

Stevens, G. & Clemens, J. D. (1993). Fluid-absent melting and the roles of fluids in the lithosphere: a slanted summary. *Chemical Geology* **108**(1–4), 1–17. https://doi.org/10.1016/0009-2541(93)90314-9.

Stuart, C. A., Piazolo, S. & Daczko, N. R. (2016). Mass transfer in the lower crust: evidence for incipient melt assisted flow along grain boundaries in the deep arc granulites of Fiordland, New Zealand. *Geochemistry, Geophysics, Geosystems* **17**(9), 3733–3753. https://doi.org/10.1002/2015GC006236.

Stuart, C. A., Daczko, N. R. & Piazolo, S. (2017). Local partial melting of the lower crust triggered by hydration through melt–rock interaction: an example from Fiordland, New Zealand. *Journal of Metamorphic Geology* **35**(2), 213–230. https://doi.org/10.1111/jmg.12229.

Stuart, C. A., Meek, U., Daczko, N. R., Piazolo, S. & Huang, J.-X. (2018). Chemical signatures of melt–rock interaction in the root of a magmatic arc. *Journal of Petrology* **59**(2), 321–340. https://doi.org/10.1093/petrology/egy029.

Torres-Rodriguez, N., Barnes, S. J., Taranovic, V., Pearce, M. A., Verrall, M. & Schoneveld, L. E. (2021). Reaction coronas at olivine–plagioclase contacts in host rocks from the Nova–Bollinger Ni–Cu–Co deposit, Albany–Fraser orogen, Western Australia: evidence of a magmatic to metamorphic continuum. *Journal of Petrology* **62**(9), egab055. https://doi.org/10.1093/petrology/egab055.

Touret, J. L. R. (1985) Fluid regime in southern Norway: The record of fluid inclusions. In: Tobi A. C. & JLR T. (eds) *The Deep Proterozoic Crust in the North Atlantic Provinces*. Dordrecht: Springer, pp.517–549.

Touret, J. L. R. & Huizenga, J. M. (2012). Fluid-assisted granulite metamorphism: a continental journey. *Gondwana Research* **21**, 224–235. https://doi.org/10.1016/j.gr.2011.07.022.

Touret, J. L. R. & Huizenga, J. M. (2020). Large-scale fluid transfer between mantle and crust during supercontinent amalgamation and disruption. *Russian Geology and Geophysics* **61**(5–6), 527–542. https://doi.org/10.15372/RGG2019128.

Touret, J. L. R. & Nijland, T. G. (2013) Prograde, peak and retrograde metamorphic fluids and associated metasomatism in upper amphibolite to granulite facies transition zones. In: Harlov D. E. & Austrheim H. (eds) *Metasomatism and the Chemical Transformation of Rock*. Berlin, Heidelberg: Springer, pp. 415–469.

Touret, J. L. R., Santosh, M. & Huizenga, J. M. (2016). High-temperature granulites and supercontinents. *Geoscience Frontiers* **7**(1), 101–113. https://doi.org/10.1016/j.gsf.2015.09.001.

Touret, J. L. R., Newton, R. C. & Cuney, M. (2019). Incipient charnockite from southern India: the role of brines. *Geoscience Frontiers* **10**, 1789–1801. https://doi.org/10.1016/j.gsf.2019.03.004.

Touret, J. L. R., Santosh, M. & Huizenga, J. M. (2022). Composition and evolution of the continental crust: retrospect and prospect. *Geoscience Frontiers* **13**, 101428. https://doi.org/10.1016/j.gsf.2022.101428.

Tribuzio, R., Renna, M. R., Antonicelli, M., Liu, T., Wu, F.-Y. & Langone, A. (2023). The peridotite-pyroxenite sequence of Rocca d'Argimonia (Ivrea-Verbano Zone, Italy): evidence for reactive melt flow and slow cooling in the lowermost continental crust. *Chemical Geology* **619**, 121315. https://doi.org/10.1016/j.chemgeo.2023.121315.

Tsunogae, T., Osanai, Y., Owada, M., Toyoshima, T., Hokada, T. & Crowe, W. A. (2003). High fluorine pargasites in ultrahigh temperature granulites from Tonagh Island in the Archean Napier Complex, East Antarctica. *Lithos* **70**(1–2), 21–38. https://doi.org/10.1016/S0024-4937(03)00087-2.

Villeneuve, M., Bellon, H., El, A., Abdelkrim, S. M., Rehault, J.-P., Olivet, J.-L. & Aghzer, A. M. (2006). Événements panafricains dans l'Adrar Souttouf (Sahara Marocain). *Comptes Rendus Geoscience* **338**(5), 359–367. https://doi.org/10.1016/j.crte.2006.02.008.

Villeneuve, M., Gärtner, A., Youbi, N., El Archi, A., Vernhet, E., Rjimati, E.-C., Linnemann, U., Bellon, H., Gerdes, A., Guillou, O., Corsini, M. & Paquette, J.-L. (2015). The southern and central parts of the "Souttoufide" Belt, Northwest Africa. *Journal of African Earth Sciences* **112**, 451–470. https://doi.org/10.1016/j.jafrearsci.2015.04.016.

Wang, T., Zheng, J., Scott, J. M., Ping, X., Ma, Q., Xiong, Q. & Zhang, S. (2022). Coronitic and symplectitic textures in meta-troctolite reveal the transition from magmatism to granulite-facies metamorphism in the early Paleozoic Tongbai Orogen, Central China. *Journal of Petrology* **63**(7), egac060. https://doi.org/10.1093/petrology/egac060.

Warren, R. G. (1983). Metamorphic and tectonic evolution of granulites, Arunta Block, Central Australia. *Nature* **305**(5932), 300–303. https://doi.org/10.1038/305300a0.

Wartho, J.-A., Rex, D. C. & Guis, P. G. (1996). Excess argon in amphiboles linked to greenschist facies alteration in the Kamila amphibolite belt, Kohistan Island Arc system, Northern Pakistan: insights from $^{40}Ar/^{39}Ar$ step-heating and acid leaching experiments. *Geological Magazine* **133**, 595–609. https://doi.org/10.1017/S0016756800007871.

White, R. W., Powell, R., Holland, T. J. B., Johnson, T. E. & Green, E. C. R. (2014). New mineral activity—composition relations for thermodynamic calculations in metapelitic systems. *Journal of Metamorphic Geology* **32**(3), 261–286. https://doi.org/10.1111/jmg.12071.

Whitney, D. L. & Evans, B. W. (2010). Abbreviations for names of rock-forming minerals. *American Mineralogist* **95**(1), 185–187. https://doi.org/10.2138/am.2010.3371.

Xiang, H. & Connolly, J. A. D. (2022). GeoPS: an interactive visual computing tool for thermodynamic modelling of phase equilibria. *Journal of Metamorphic Geology* **40**(2), 243–255. https://doi.org/10.1111/jmg.12626.

Deltech Furnaces

Sustained operating temperatures to 1800° Celsius

www.deltechfurnaces.com

Gas Mixing System

An ISO 9001:2015 certified company

Custom Vertical Tube

ASME NQA-1 2008 Nuclear Quality Assurance

Standard Vertical Tube

Control systems are certified by Intertek UL508A compliant

Bottom Loading Vertical Tube